

Modeling the Ly α transit absorption of the hot Jupiter HD 189733b

P. Odert^{1,2}, N. V. Erkaev^{3,4}, K. G. Kislyakova^{5,1}, H. Lammer¹, A. V. Mezentsev⁴, V. A. Ivanov⁴,
L. Fossati¹, M. Leitzinger², D. Kubyschkina¹, and M. Holmström⁶

¹ Space Research Institute, Austrian Academy of Sciences, Schmiedlstraße 6, A-8042 Graz, Austria

² Institute of Physics/IGAM, University of Graz, Universitätsplatz 5, A-8010 Graz, Austria
e-mail: petra.odert@uni-graz.at

³ Institute of Computational Modelling of the Siberian Branch of the Russian Academy of Sciences, 660036 Krasnoyarsk, Russian Federation

⁴ Siberian Federal University, 660041 Krasnoyarsk, Russian Federation

⁵ Institute for Astronomy, University of Vienna, Türkenschanzstraße 17, A-1180 Vienna

⁶ Swedish Institute of Space Physics, PO Box 812, SE-98128 Kiruna, Sweden

Received ???; accepted ???

ABSTRACT

Context. Hydrogen-dominated atmospheres of hot exoplanets expand and escape hydrodynamically due to the intense heating by the X-ray and extreme ultraviolet (XUV) irradiation of their host stars. Excess absorption of neutral hydrogen has been observed in the Ly α line during transits of several close-in gaseous exoplanets, indicating such extended atmospheres.

Aims. For the hot Jupiter HD 189733b, this absorption shows temporal variability. Variations in stellar XUV emission and/or variable stellar wind conditions have been invoked to explain this effect.

Methods. We apply a 1D hydrodynamic planetary upper atmosphere model and a 3D MHD stellar wind flow model to study the effect of variations of the stellar XUV irradiation and wind conditions at the planet's orbit on the neutral hydrogen distribution, including the production of energetic neutral atoms (ENAs), and the related Ly α transit signature.

Results. We are able to reproduce the Ly α absorption observed in 2011 with a stellar XUV flux of 1.8×10^4 erg cm⁻² s⁻¹, rather typical activity conditions for this star. Flares with parameters similar to the one observed 8 h before the transit are unlikely to have caused a significant modulation of the transit signature. We find that the resulting Ly α absorption is dominated by atmospheric broadening, whereas the contribution of ENAs is **negligible, as they are formed inside the bow shock from decelerated wind ions that are heated to high temperatures. Thus, within our modeling framework and assumptions, we find an insignificant dependence of the absorption on the stellar wind parameters.**

Conclusions. Since the transit absorption can be modeled with typical stellar XUV and wind conditions, it is possible that the non-detection of the absorption in 2010 was affected by less-typical stellar activity conditions, such as a very different magnitude and/or shape of the star's spectral XUV emission, or temporal/spatial variations in Ly α affecting the determination of the transit absorption.

Key words. planets and satellites: atmospheres – planets and satellites: individual: HD 189733b – stars: activity – ultraviolet: planetary systems – hydrodynamics – magnetohydrodynamics (MHD)

1. Introduction

The first observational evidence of an expanding and escaping exoplanetary atmosphere was the Ly α transit absorption detected for the hot Jupiter HD 209458b (Vidal-Madjar et al. 2003). Subsequently, more observations of excess absorption in Ly α and UV lines of other elements succeeded, the most prominent ones being the hot Jupiters HD 209458b (Vidal-Madjar et al. 2004, 2008, 2013; Ben-Jaffel 2007, 2008; Ballester et al. 2007; Ehrenreich et al. 2008; Linsky et al. 2010; Ben-Jaffel & Sona Hosseini 2010; Ballester & Ben-Jaffel 2015), HD 189733b (Lecavelier des Etangs et al. 2010, 2012; Bourrier et al. 2013; Ben-Jaffel & Ballester 2013), WASP-12b (Fossati et al. 2010; Haswell et al. 2012), 55 Cnc b (Ehrenreich et al. 2012) and the warm Neptune GJ 436b (Kulow et al. 2014; Ehrenreich et al. 2015; Lavie et al. 2017). Numerous hydrodynamic models for hot Jupiter upper atmospheres were developed, aiming to explain the observations (Yelle 2004; Tian et al. 2005; García Muñoz 2007; Penz et al. 2008; Stone & Proga 2009; Murray-Clay et al. 2009; Guo 2011, 2013; Koskinen et al. 2013; Shaikhislamov et al. 2014; Salz et al. 2016a; Guo & Ben-Jaffel 2016; Erkaev et al. 2016;

Khodachenko et al. 2017; Debrecht et al. 2018). Other studies employed Direct Simulation Monte Carlo (DSMC) models which include the generation of energetic neutral atoms (ENAs) due to interaction with the stellar wind and take into account the effects of radiation pressure on the shaping of the large hydrogen clouds (Holmström et al. 2008; Ekenbäck et al. 2010; Bourrier & Lecavelier des Etangs 2013; Kislyakova et al. 2014; Bourrier et al. 2015, 2016).

It is therefore important to study the interaction of the expanding planetary atmosphere with the magnetized stellar wind. The escaping atmospheric particles mixed with stellar wind plasma can have a strong influence on the wind plasma parameters in the vicinity of the planet. The main effect of an intrinsic planetary magnetic field on atmospheric escape is to suppress the outflow and to make it highly anisotropic (Adams 2011; Trammell et al. 2011, 2014; Owen & Adams 2014; Khodachenko et al. 2015). Many studies investigated the interaction between a close-in planet and its host star's wind, but some of them neglected magnetic fields and all just considered a purely hydrodynamic interaction (Stone & Proga 2009; Bisikalo et al. 2013;

Tremblin & Chiang 2013; Christie et al. 2016). Other studies, instead, applied MHD models (Cohen et al. 2011; Matsakos et al. 2015; Tilley et al. 2016), but employing mostly simplified descriptions of the planetary wind. Shaikhislamov et al. (2016) used a 2D multi-fluid code to study the interaction of a non-magnetized HD 209458b-like hot Jupiter with the stellar wind, taking into account heating by the stellar X-ray and extreme ultraviolet (XUV) flux and hydrogen photochemistry to self-consistently model the planetary outflow. However, they did not include the interplanetary magnetic field (IMF) and its effect on the formation of the planetary obstacle. This was addressed by Erkaev et al. (2017), who used a 1D hydrodynamic planetary upper atmosphere model in combination with a 3D MHD stellar wind flow model to investigate the build-up of a planetary obstacle produced by the interaction of the partially ionized planetary wind with the plasma flow of a magnetized stellar wind.

The hot Jupiter HD 189733b was discovered by Bouchy et al. (2005) on the basis of both radial velocity and photometric transit observations. The most recent determinations of its mass and radius are $1.13 M_{\text{Jup}}$ and $1.13 R_{\text{Jup}}$, based on *Gaia* parallaxes (Stassun et al. 2017). The host star HD 189733 has a spectral type of K2V (Gray et al. 2003) and is the primary of a double system, with a mid-M dwarf companion located at a projected separation of ~ 216 AU (Bakos et al. 2006). The activity level and rotation period (11.95 d; Henry & Winn 2008) of HD 189733, comparable to the similar K star ϵ Eri, correspond to an age of 1-2 Gyr (Poppenhaefer & Wolk 2014). However, the accompanying M dwarf is rather inactive and has therefore an estimated age of >5 Gyr. It was therefore suggested that HD 189733 may show the high rotation rate and associated high level of magnetic activity due to interactions with its hot Jupiter (Poppenhaefer & Wolk 2014). Independent of the reasons of the host star's high activity level, HD 189733b is therefore exposed to intense stellar XUV emission, and possibly also to a dense and fast stellar wind. This may lead to enhanced atmospheric loss, which is also indicated by UV transit observations. Moreover, Pillitteri et al. (2015) suggested that observed FUV variability could stem from accretion of matter from the planet onto the star. Route (2019) analyzed multi-wavelength data of HD 189733 to find possible indications of star-planet interaction, but could not identify a clear relation between the stellar activity characteristics and the planetary orbital phases.

Lecavelier des Etangs et al. (2010) observed three transits and detected an absorption of $5.05 \pm 0.75\%$ in the unresolved $\text{Ly}\alpha$ line, significantly higher than the absorption by the planetary disk at optical wavelengths. Later, Lecavelier des Etangs et al. (2012) obtained $\text{Ly}\alpha$ observations with higher spectral resolution at two different epochs (April 2010, September 2011). While during the first epoch no excess absorption could be detected (just absorption of the total flux comparable to the 2.4% absorption by the planetary disk at optical wavelengths, no spectrally resolved absorption), they found absorption of $14.4 \pm 3.6\%$ (i.e. $12.3 \pm 3.6\%$ excess absorption) in the blue wing of the line in a velocity range of -230 to -140 km s^{-1} , indicating absorbing material moving away from the star. They also found absorption in the red wing from 60 to 110 km s^{-1} of $7.7 \pm 2.7\%$, i.e. $5.5 \pm 2.7\%$ excess, indicating absorbing material moving towards the star, but this detection was not statistically significant. Using Monte Carlo simulations, Bourrier & Lecavelier des Etangs (2013) were able to reproduce the excess absorption observed in 2011 with a neutral hydrogen outflow rate of $4 \times 10^8 - 10^{11}$ g s^{-1} , an ionizing flux of 6–23 times the solar value, and a stellar wind with a temperature of 3×10^4 K, a velocity of 200 ± 20 km s^{-1} , and a density between $10^3 - 10^7$ cm^{-3} . Lecavelier des Etangs et al.

(2012) suggested that the absence of excess absorption in 2010 could be due to a much lower escape rate or a less dense stellar wind. They explained the discrepancy between the observations in 2010 and 2011 by the influence of a flare that occurred ~ 8 h prior to the transit in 2011. Bourrier et al. (2013) presented a more detailed analysis of the 2011 observations, reaching similar conclusions.

Further attempts were made to explain the temporal variability of the $\text{Ly}\alpha$ transit absorption of HD 189733b. Guo & Ben-Jaffel (2016) investigated the effect of the stellar XUV spectral energy distribution (SED) on atmospheric profiles and mass-loss rate. They found that the mass-loss rate is mainly determined by the total absorbed energy, whereas the ionization is strongly affected by the SED. For SEDs dominated by the low-energy part of the spectrum, the H/H^+ transition moves closer to the planet, and the amount of H atoms at a certain altitude can differ by 1-2 orders of magnitude, in comparison to SEDs dominated by the high-energy part. They used the method of Ben-Jaffel (2008) to investigate the differences in absorption signature depending on the stellar XUV SED and found that they can explain the differences in observations between 2010 and 2011 by assuming a harder stellar spectrum in 2011. The model of Ben-Jaffel (2008) assumes an extended thermosphere with an absorption profile broadened by natural broadening and does not include non-thermal H populations like ENAs. Therefore, the resulting transmission spectrum is symmetric around the $\text{Ly}\alpha$ line center and does not reproduce the localized absorption at higher velocities in the blue wing. Recently, Chadney et al. (2017) studied the influence of flares of the upper atmospheres and escape rates of hot Jupiters. They found a maximum mass-loss enhancement of about a factor of two, and much less if the limited duration of the radiation enhancement during a flare is taken into account. However, they suggested that an extreme proton event associated with the flare could have led to sufficiently enhanced escape.

Ben-Jaffel & Ballester (2013) reported a $6.4 \pm 1.8\%$ absorption in O I and a marginal detection of early-ingress C II absorption. However, they could not exclude that the latter had a stellar or instrumental origin. Transit absorption in the $\text{H}\alpha$ line was also detected in several observations, as well as a pre-transit signature (Jensen et al. 2012; Cauley et al. 2015, 2016, 2017b). However, both in- and pre-transit absorption signatures were highly variable in time and strongly affected by stellar activity, making their interpretation difficult (Barnes et al. 2016; Cauley et al. 2017a; Kohl et al. 2018). Furthermore, a 6-8% transit absorption in X-rays was reported by Poppenhaefer et al. (2013), but more observations with higher sensitivity are needed to confirm this result (Marin & Grosso 2017).

In this paper, we will investigate the possible causes for the variations of the $\text{Ly}\alpha$ transit absorption of HD 189733b. To achieve this, we will model the structure of the upper atmosphere taking into account stellar XUV heating and the associated mass-loss under both quiescent and flaring conditions. Then, we will model the interaction between the stellar wind and the atmosphere and the related production of ENAs and its impact on the UV transit signature. In section 2, we describe the hydrodynamic model, and show the resulting upper atmosphere profiles and planetary mass-loss rates in section 3. In section 4, we describe the MHD flow model and show the stellar wind flow maps. In section 5, we compute the $\text{Ly}\alpha$ absorption for the various cases and compare it to the observations. In section 6, we discuss the results and compare them with other studies. Conclusions are presented in section 7.

2. Hydrodynamic upper atmosphere modeling

2.1. Model description

The hydrodynamic model solves the time-dependent system of the equations of mass, momentum and energy conservation in 1D spherical geometry along the star-planet line,

$$\frac{\partial \rho r^2}{\partial t} + \frac{\partial \rho u r^2}{\partial r} = 0 \quad (1)$$

$$\frac{\partial \rho u r^2}{\partial t} + \frac{\partial (\rho u^2 + p) r^2}{\partial r} = g \rho r^2 + 2 p r \quad (2)$$

$$\frac{\partial E_{\text{th}} r^2}{\partial t} + \frac{\partial E_{\text{th}} u r^2}{\partial r} = Q r^2 + \frac{\partial}{\partial r} \left(\kappa r^2 \frac{\partial T}{\partial r} \right) - p \frac{\partial u r^2}{\partial r}. \quad (3)$$

The gas parameters ρ , u , T , $E_{\text{th}} = p/(\gamma - 1)$ are the mass density, velocity, temperature, and thermal energy of the upper atmosphere. The gas pressure $p = \rho R T / \mu$, with the mean molecular weight μ and the gas constant R . The distance from the planet's center is r and t is the time. For the specific heat ratio γ we adopt 5/3 for monatomic gas. The gravitational force $g = -\partial\Phi/\partial r$ is derived from the Roche potential Φ along the star-planet line

$$\Phi = -\frac{GM_p}{r} - \frac{GM_*}{a-r} - \frac{G(M_p + M_*)}{2a^3} \left(a \frac{M_*}{M_p + M_*} - r \right)^2 \quad (4)$$

(e.g. García Muñoz 2007). Here, G is the gravitational constant, M_p the planet's mass, M_* the stellar mass, and a the star-planet separation. The right hand side of Eq. 3 includes the net volume heating rate Q and thermal conduction, which are both described in section 2.2.

The simulations assume an atmosphere composed entirely of hydrogen, i.e. we neglect helium and other heavier elements, which are minor compared to hydrogen. For HD 189733b, we also neglect molecular species which are present in the lower atmosphere, but the strong ionization of the upper atmosphere is expected to destroy them efficiently (cf. Guo & Ben-Jaffel 2016, and Appendix C). Therefore, we only consider hydrogen atoms (H) and protons (H⁺). The production of H⁺ is calculated as

$$\frac{\partial n_{\text{H}^+}}{\partial t} + \frac{1}{r^2} \frac{\partial n_{\text{H}^+} u r^2}{\partial r} = \alpha_{\text{ion}} n_{\text{H}} - \alpha_{\text{rec}} n_{\text{H}^+} n_{\text{e}} + \alpha_{\text{col}} n_{\text{H}} n_{\text{e}} \quad (5)$$

where α_{ion} is the photoionization rate, α_{rec} the radiative recombination rate, and α_{col} the collisional ionization rate (all quantities in cgs units). The parameters n_{H} , n_{H^+} , n_{e} are the number densities of neutral hydrogen atoms, protons, and electrons, respectively. We assume quasi-neutrality, $n_+ = n_{\text{e}}$. The photoionization rate is given by

$$\alpha_{\text{ion}}(r) = \sum_{\lambda} \sigma_{\text{ion},\lambda} \frac{F_{\text{XUV},\lambda} e^{-\tau_{\lambda}(r)}}{E_{\lambda}}, \quad (6)$$

where $\sigma_{\text{ion}}(\lambda)$ is the photoionization cross-section, $F_{\text{XUV}}(\lambda)$ the spectral XUV flux at the planet's orbit outside of the atmosphere, $\tau_{\lambda}(r)$ the optical depth at distance r from the planet's center, and E_{λ} the photon energy (e.g. Murray-Clay et al. 2009). We compute the average photoionization cross-sections per spectral bin from the fits of Verner et al. (1996) and adopt photon energies corresponding to the central wavelengths of the bins. The recombination and collisional ionization rates are taken from Glover & Jappsen (2007). For the former, we adopt the case B¹ coefficient

¹ The case B recombination coefficient takes into account that photons emitted by recombinations to the ground level immediately ionize a nearby atom and do not effectively contribute to recombination.

$$\alpha_{\text{rec}} = 2.753 \times 10^{-14} \left(\frac{315614}{T} \right)^{1.5} \left[1 + \left(\frac{115188}{T} \right)^{0.407} \right]^{-2.242}, \quad (7)$$

while the latter is given by

$$\alpha_{\text{col}} = \exp \left(-3.271396786 \times 10^1 + 1.35365560 \times 10^1 \theta \right) \quad (8)$$

$$- 5.73932875 \times 10^0 \theta^2 + 1.56315498 \times 10^0 \theta^3 \quad (9)$$

$$- 2.87705600 \times 10^{-1} \theta^4 + 3.48255977 \times 10^{-2} \theta^5 \quad (10)$$

$$- 2.63197617 \times 10^{-3} \theta^6 + 1.11954395 \times 10^{-4} \theta^7 \quad (11)$$

$$- 2.03914985 \times 10^{-6} \theta^8, \quad (12)$$

where $\theta = \ln T_{\text{e}}$ with the electron temperature T_{e} in eV.

The system of hydrodynamic equations is normalized as in Erkaev et al. (2016) and solved using the MacCormack scheme (MacCormack 1969). We slightly modified the code in comparison to the version described in Erkaev et al. (2016). Mainly, we extended the scheme with the Total Variation Diminishing (TVD) property. The code extensions are described in detail in Appendix A. Another modification is introduced here. Our initial modeling results of HD 189733b yielded strong unphysical behavior close to the lower boundary of the computational domain, specifically an increasing velocity towards r_0 , which violated the mass conservation. This was mainly due to the fact that the outflow of HD 189733b's upper atmosphere remains subsonic up to the L1 point, and is therefore highly subsonic close to the lower boundary. Schemes like the MacCormack method are not well suited for such flows. Since for highly subsonic flows the kinetic energy is very small, we solve for the thermal energy instead of the total energy as in Erkaev et al. (2016). We discretized the third term on the right-hand side of Eq. 3 like the flux terms in both MacCormack steps.

The code evolves the system of equations until a steady-state solution is achieved. We assume that this condition is fulfilled when the mass flux throughout the simulation domain is approximately constant, i.e. mass conservation is fulfilled to 1%. Moreover, we compare the total heating and cooling rates to confirm the energy conservation (cf. Appendix A.2).

2.2. Heating and cooling processes

The main source of heating is the stellar XUV radiation. The XUV volume heating rate can be written as

$$Q_{\text{XUV}}(r) = \sum_{\lambda} \eta_{\text{ph}} \sigma_{\text{ion},\lambda} n_{\text{H}}(r) \frac{(E_{\lambda} - 13.6 \text{eV})}{E_{\lambda}} F_{\text{XUV},\lambda} \frac{\exp(-\tau_{\lambda}(r))}{1 + \alpha \tau_{\lambda}(r)}, \quad (13)$$

where the term $1 + \alpha \tau$ takes into account 2D effects of the energy absorption in an approximative way (Sekiya et al. 1980). The optical depth is calculated as

$$\tau_{\lambda}(r) = \int_r^{\infty} \sigma_{\text{ion},\lambda} n_{\text{H}}(r) dr. \quad (14)$$

We adopt a constant photoelectron heating efficiency η_{ph} of 50%. This is intermediate between the values calculated for Jupiter (63%; Waite et al. 1983) and HD 209458b (20-40%; Shematovich et al. 2014), and was adopted by studies similar to ours (Shaikhislamov et al. 2014, 2016). The heating rate from Eq. 13

yields very similar results to the 2D method described in previous papers (Erkaev et al. 2013, 2016) for $\alpha = 4$. We revert here to a 1D calculation of Q_{XUV} because we introduced usage of XUV spectra here, motivated by the previously demonstrated effects of the assumed SED (Guo & Ben-Jaffel 2016). This also allows inclusion of X-ray heating, which is important for hot Jupiters. The calculation of a non-gray 2D heating function is computationally more expensive, but the resulting Q_{XUV} is very similar to the 1D method shown in Eq. 13 (see Appendix B for a comparison). The adopted XUV spectra are described in section 2.4.

We include several cooling processes, namely Lyman- α cooling (H excitation), radiative recombination, free-free emission (Bremsstrahlung), and collisional ionization. All cooling rates were taken from Glover & Jappsen (2007) and are given in cgs units. The Lyman- α cooling rate

$$\Lambda_{\text{Ly}\alpha} = 0.1 \times 7.5 \times 10^{-19} \left(1 + \sqrt{\frac{T}{10^5}}\right)^{-1} \exp\left(-\frac{118348}{T}\right) n_e n_{\text{H}} \quad (15)$$

was multiplied by a factor 0.1, as suggested by Koskinen et al. (2013) based on detailed calculations of the photon escape probability in the upper atmosphere of HD 209458b (Menager et al. 2013), to account for the optical thickness. The cooling rate by radiative recombination is

$$\Lambda_{\text{rec}} = 1.38 \times 10^{-16} T \alpha_{\text{rec}} n_e n_{\text{H}^+}, \quad (16)$$

by collisional ionization

$$\Lambda_{\text{col}} = 2.179 \times 10^{-11} \alpha_{\text{col}} n_e n_{\text{H}}, \quad (17)$$

and by free-free emission

$$\Lambda_{\text{ff}} = 1.426 \times 10^{-27} T^{1/2} g_{\text{ff}} n_e n_{\text{H}^+}, \quad (18)$$

with $g_{\text{ff}} = 0.79464 + 0.1243 \log_{10}(T)$. The net heating rate is then computed via

$$Q_{\text{net}} = Q_{\text{XUV}} - (\Lambda_{\text{Ly}\alpha} + \Lambda_{\text{rec}} + \Lambda_{\text{col}} + \Lambda_{\text{ff}}) \quad (19)$$

Thermal conduction is also included in the model. The conductivity coefficient is calculated as $\kappa = n^{-1} \sum_j n_j \kappa_j$ (e.g. García Muñoz 2007), where n_j are the number densities of the constituents and $\kappa_j = A_j T^{s_j}$, where A_j , s_j are the fitting parameters of the individual conductivities. We adopt $A_{\text{H}} = 379$, $A_{\text{H}^+} = 7.37 \times 10^{-8}$, $A_{\text{e}} = 1.2 \times 10^{-6}$, $s_{\text{H}} = 0.69$, and $s_{\text{H}^+} = s_{\text{e}} = 2.5$ (García Muñoz 2007). Note that the contribution of H^+ is negligible compared to that of the electrons.

We compute the total heating and cooling rates to confirm the energy conservation in our code. The total cooling rate consists of the four explicitly included cooling processes described above, in addition to adiabatic cooling, which is implicitly included in Eq. 3. Adiabatic cooling includes the contributions of advection

$$\Lambda_{\text{ad}} = \frac{1}{r^2} \frac{\partial E_{\text{th}} u r^2}{\partial r}, \quad (20)$$

and expansion

$$\Lambda_{\text{ex}} = \frac{p}{r^2} \frac{\partial (u r^2)}{\partial r} \quad (21)$$

(e.g. Salz et al. 2016a). The total heating rate is mostly dominated by XUV heating (Eq. 13), but locally advection can also contribute significantly, especially at larger heights. Note that conduction can also both cool and heat the gas, but we found it to be negligible, because its contribution to the energy balance significantly smaller than the other processes on this specific planet.

2.3. Initial and boundary conditions

The simulation domain extends from the planet's optical transit radius $r_0 = R_p$ to $r_1 = 4.5R_p$. The upper boundary lies near the L1 point $R_{\text{L1}} = (\mu - \mu^2/3)a \sim 4.3R_p$, where $\mu = (M_p/(3M_*))^{1/3}$ (e.g. Erkaev et al. 2007). Note that due to the high gravity of HD 189733b the distance between R_p and typical mesopause pressure levels is very small. We use a non-uniform grid $r_i = r_1^{i/(N-1)}$ with typically $N = 5000$ grid points. This high number is necessary because of the steep density gradient and the small velocities near the inner boundary that are present on this planet.

At the lower, subsonic inflow boundary, we fix the values for temperature T_0 and number density n_0 . For the temperature, we adopt the equilibrium temperature of 1200 K (cf. Section 2.4) and for the number density a value of 10^{15} cm^{-3} (cf. Table 1). This corresponds to a pressure of 0.16 mbar. Changing T_0 to 800 K or 1600 K, respectively, decreases or increases the mass-loss rate by $\sim 10\%$ and affects the atmospheric profiles negligibly (cf. Section 3.1). We checked that the assumed density is chosen large enough so that the optical depth in all XUV spectral bins exceeds 10. Only then the stellar XUV flux is completely absorbed in the simulation domain and the resulting mass-loss rates do not depend strongly on the choice of n_0 . Smaller values of n_0 would lead to significant ionization below the optical transit radius, which would be inconsistent with its measurement (see section 6.3). For runs which result in very subsonic flows we set $u=0$ at the lower boundary. This does not affect the results, but improves the speed of convergence and the quality of the atmospheric profiles (e.g. Shaikhislamov et al. 2014). At the upper boundary we adopt free outflow (i.e. zero gradient) conditions on all parameters.

As initial conditions we use constant temperature and a monotonically increasing velocity profile $u(r) = 0.1(r - 1)$. For the number density we assume hydrostatic conditions $n(r) = \exp(\Phi(r) - \Phi(r_0))$ modified in the upper region to $n(r) \propto 1/r^2$. This is necessary because of the steep density gradient of the hydrostatic solution for this high gravity planet. Initially, we assume that the atmosphere consists only of atomic H, i.e. $n_{\text{H}^+}(r) = 0$. For most runs we start from previous solutions for similar parameter sets to reduce the computing time. We consider a run as properly converged when the mass flux $\rho u r^2$ is spatially constant within 1% throughout the computational domain (excluding a small region near the planet where the mass flux may drop to zero because of numerical reasons; cf. Fig. A.1). We checked that the adopted initial conditions and the chosen resolution of the grid do not affect the results. **Moreover, we verified that the chosen location of the upper boundary does not affect the results.**

2.4. Adopted physical parameters

The adopted planetary and stellar parameters (Table 1) were taken from Stassun et al. (2017) and are based on the accurate parallaxes from the first data release of *Gaia* (Gaia Collaboration et al. 2016). The distance d , stellar mass M_* and radius R_* , stellar bolometric flux at Earth F_{bol} , planetary mass M_p and radius R_p , as well as the orbital inclination i were taken from their study. The orbital separation a was calculated from their quoted value of the parameter $a/R_* = 8.84 \pm 0.27$ and the stellar radius. The average orbital velocity is therefore 151 km s^{-1} , consistent with the maximum orbital radial velocity of $154_{-3}^{+4} \text{ km s}^{-1}$ measured by de Kok et al. (2013). Using the measured bolometric stellar flux, we find an equilibrium temperature $T_{\text{eq}} = (F_{\text{bol}}(1 - A)/(f\sigma))^{1/4}$ of 1200 K, assuming full

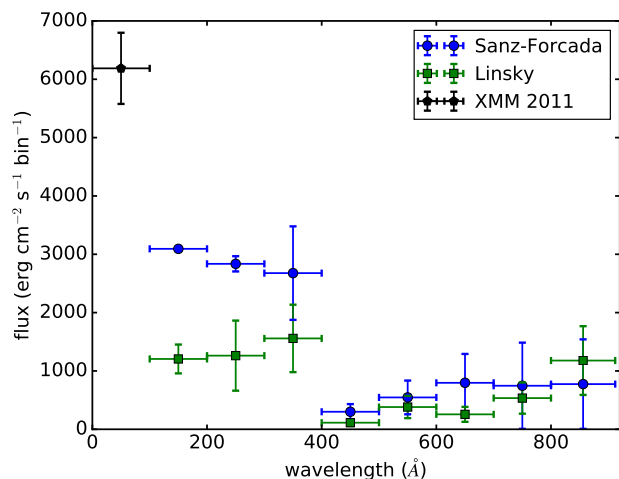


Fig. 1. XUV (5–912 Å) spectral flux at the orbit of HD 189733b in bins of ~ 100 Å, obtained with the methods of L14 and SF11. The X-ray flux is an average value outside of flares obtained with XMM-Newton in 2011 (Pillitteri et al. 2014).

redistribution ($f = 4$) and zero albedo ($A = 0$). Here, σ is the Stefan-Boltzmann constant. This is similar to, but slightly higher than, the apparent effective dayside temperature of 1163 ± 37 K (Schwartz et al. 2017). Such small differences in the adopted T_{eq} do not affect our results.

The XUV flux of HD 189733 is highly variable due to the high activity of this star. Observed X-ray luminosities are in a range of $1.1\text{--}2.8 \times 10^{28}$ erg s $^{-1}$, which are partly obtained from different instruments with slightly different bandpasses, but were also measured at different epochs (Hünsch et al. 1999; Pillitteri et al. 2010, 2011, 2014; Lecavelier des Etangs et al. 2012; Poppenhaeger et al. 2013). Since the EUV part of the stellar spectrum is largely unobservable due to absorption by the interstellar medium (ISM), it has to be inferred indirectly. We compare two approaches to estimate the unobservable EUV spectrum. First, we use the scaling relations from Linsky et al. (2014, hereafter L14) based on the intrinsic Ly α flux, as derived from observations of the short-wavelength part of the EUV range (<400 Å) in nearby stars, and solar models for >400 Å. Since also Ly α fluxes are affected by the ISM absorption, the intrinsic stellar line profile needs to be reconstructed. From HST observations of HD 189733 in 2010, the intrinsic Ly α flux at Earth amounts to 7.5×10^{-13} erg cm $^{-2}$ s $^{-1}$ with quoted uncertainties of 15–30% (France et al. 2013). The reconstructed line profile from Bourrier et al. (2013) for the 2011 observations corresponds to a flux of 6.8×10^{-13} erg cm $^{-2}$ s $^{-1}$, slightly lower, but consistent with France et al. (2013), considering the typical uncertainties of the reconstruction. We adopt the latter value because we will focus on modeling the 2011 observations. This flux value, together with the scalings from L14, gives a total EUV (100–912 Å) flux at the planet’s orbit of 6.5×10^3 erg cm $^{-2}$ s $^{-1}$ with a spectral energy distribution shown in Fig. 1.

Second, we examine the synthetic spectrum from the X-exoplanets² database (Sanz-Forcada et al. 2010, 2011, hereafter SF11). These authors used observed X-ray and UV spectra, reconstructed the emission measure distribution, and used this as input for coronal models to infer the unknown EUV part of the

Table 1. Stellar and planetary parameters from Stassun et al. (2017). The orbital distance a was calculated from their quoted value of a/R_* and R_* .

Parameter	Value
d (pc)	19.84 ± 0.09
M_* (M_{\odot})	0.79 ± 0.08
R_* (R_{\odot})	0.75 ± 0.01
F_{bol} (erg cm $^{-2}$ s $^{-1}$)	$2.68 \times 10^{-8} \pm 3.94 \times 10^{-10}$
M_{p} (M_{Jup})	1.13 ± 0.08
R_{p} (R_{Jup})	1.13 ± 0.01
a (AU)	0.031 ± 0.001
i ($^{\circ}$)	85.71

spectrum. We show their synthetic spectrum with the same binning as for L14 in Fig. 1. The errorbars in x -direction give the width of the bins (100 Å), those along the y -axis the estimated flux errors based on the uncertainties quoted in the respective studies. It is apparent that the SF11 fluxes are systematically higher than the L14 ones (except for the 800–912 Å bin, which is likely due to the peak of the Lyman continuum, which is included in the solar models used by L14, but not in SF11). The $\lambda > 300$ Å range is consistent within the estimated uncertainties. The $\lambda < 300$ Å range differs significantly. This could be due to shortcomings in the models of either study, and/or the fact that the X-ray spectrum used by SF11 was taken at a different epoch (2007) than the Ly α flux we adopted for the L14 method (2011). Some intrinsic stellar variability could therefore also be a cause of the differences. Pillitteri et al. (2014) give a comparison of the X-ray fluxes obtained with XMM/Newton at different epochs (2007=SF11, 2009, 2011, 2012) and the associated temperatures and emission measures. In 2011, the temperatures were comparable, but the emission measures and X-ray fluxes were higher than in 2007. However, the 2011 X-ray observations were not taken at the same time as the Ly α observations. Simultaneous observations with *Swift*/XRT during the 2011 transit yield an X-ray (0.3–3 keV) flux of 3.6×10^{-13} erg cm $^{-2}$ s $^{-1}$ (Lecavelier des Etangs et al. 2012), whereas the 2007 XMM/Newton (0.12–2.48 keV) flux is 3.4×10^{-13} erg cm $^{-2}$ s $^{-1}$ (SF11) and for 2011 $3.2\text{--}3.9 \times 10^{-13}$ erg cm $^{-2}$ s $^{-1}$ (excluding the flare; Pillitteri et al. 2014). Hereafter we adopt the average XMM value (excluding the flare) from 2011, 3.55×10^{-13} erg cm $^{-2}$ s $^{-1}$ (Pillitteri et al. 2014), which amounts to 6.2×10^3 erg cm $^{-2}$ s $^{-1}$ at the orbit of HD 189733b.

The total EUV fluxes (100–912 Å) at the planet’s orbit obtained with the two different methods are 6.5×10^3 erg cm $^{-2}$ s $^{-1}$ for the L14 method and 1.2×10^4 erg cm $^{-2}$ s $^{-1}$ for SF11. As a comparison, we also calculate the total EUV flux using the method of Chadney et al. (2015), which uses a scaling with X-ray flux. With our adopted X-ray flux, we obtain an orbital EUV flux of 1.1×10^4 erg cm $^{-2}$ s $^{-1}$, comparable to SF11. We note, however, that the Chadney et al. (2015) scaling is based on the SF11 coronal models. On the basis of the discrepancies between the different reconstruction methods, we estimate that the uncertainty in EUV flux is at least a factor of two. The total XUV (5–912 Å) fluxes at the planet’s orbit from each method amount to 1.3×10^4 and 1.8×10^4 erg cm $^{-2}$ s $^{-1}$ for L14 and SF11, respectively (cf. Table 2). We explore the influence of XUV flux variations further in section 3.2, where we model the influence of a flare.

² <http://sdc.cab.inta-csic.es/xexoplanets/jsp/homepage.jsp>

Table 2. Modeled mass-loss rates \dot{M} for different stellar XUV fluxes/spectra and lower boundary parameters (number density n_0 , temperature T_0). Rows 3 and 4 give the results for the X-ray and XUV flares, respectively (see section 3.2).

F_{XUV} (erg cm ⁻² s ⁻¹)	XUV	n_0 (cm ⁻³)	T_0 (K)	\dot{M} (g s ⁻¹)
1.80×10^4	SF11	10^{15}	1200	5.4×10^{10}
1.27×10^4	L14	10^{15}	1200	2.5×10^{10}
3.65×10^4	SF11+X	10^{15}	1200	8.7×10^{10}
7.18×10^4	SF11+XUV	10^{15}	1200	1.2×10^{11}
1.80×10^4	SF11	10^{15}	800	4.8×10^{10}
1.80×10^4	SF11	10^{15}	1600	6.1×10^{10}
1.80×10^4	SF11	5×10^{15}	1200	1.7×10^{11}

3. Hydrodynamic modeling results

3.1. Atmospheric profiles and mass-loss rate

Here we show the upper atmosphere profiles obtained using both the SF11 and L14 XUV spectra (Fig. 2). The isotropic (i.e. maximum) mass-loss rates $\dot{M} = 4\pi r^2 \rho u$ (assuming that the star-planet line value is representative for entire atmosphere) are 5.4×10^{10} and 2.5×10^{10} g s⁻¹ for SF11 and L14, respectively (Table 2).

In Fig. 2 we show the atmospheric profiles for number density, velocity, temperature and ionization fraction (n_{H^+}/n) for both the SF11 and L14 reconstructions of the stellar XUV spectra. The results are rather similar for both spectra, although all parameters are slightly lower for the L14 spectra because of the lower total XUV flux. The number density is dominated by neutral H below about $1.85R_p$ and by H⁺ above. The transition from the H-dominated atmosphere to one dominated by H⁺ occurs where the ionization fraction exceeds 0.5. The outflow reaches the sonic speed just slightly below the L1 point at $4.3R_p$ in both cases, whereas it already exceeds the escape velocity at points that are $\sim 0.3R_p$ closer to the planet. The temperature reaches a maximum of $\sim 1.1 \times 10^4$ K at $\sim 2R_p$ for SF11, whereas the maximum temperature is slightly lower for L14 and located closer to the planet.

The results are only considered to be valid well within the Roche lobe and less reliable close to or above the Roche lobe where 3D effects become important (e.g. Bisikalo et al. 2013). Moreover, it is important to check if the outflow remains collisional within our computational domain so that the hydrodynamic treatment can be justified. The transition level to the collisionless regime is commonly taken as Knudsen number $Kn = \Lambda/X = 1$, where $\Lambda = 1/(n\sigma_{\text{col}})$ is the mean free path and X is an appropriate system scale, e.g. the scale height $H = kT/(m_p g)$ for regions close to the planet, or the planetary radius for more distant regions (Shaikhislamov et al. 2014). For the collision cross-section σ_{col} we adopt the H-H⁺ charge exchange cross-section ($\sim 2 \times 10^{-15}$ cm²; e.g. Lindsay & Stebbings 2005), which is the appropriate choice for partially ionized hydrogen atmospheres (Guo 2011; Salz et al. 2016a; Shaikhislamov et al. 2016). Taking for X either H or R_p we find that $Kn \ll 1$ inside our computational domain, justifying the hydrodynamic approach.

Figure 3 details the individual heating and cooling processes in our model for the SF11 run. One can see that the main heating source is the stellar XUV radiation, although advection contributes to heating in the upper atmosphere. Advection cools the gas at lower heights, although it is much smaller than the cooling from expansion. Expansion is even the dominant cooling mechanism above about $2.5R_p$. Radiative cooling is also very important

for HD 189733b and is dominated by Ly α emission close to the planet, whereas in the upper layers recombination radiation and free-free emission are more important. Both collisional ionization and conduction (not shown) are negligible cooling mechanisms.

We calculate the heating efficiency using two different definitions commonly found in the literature. First, we calculate the heating efficiency $\eta_{\text{XUV}}(r)$ defined as the ratio of the XUV volume heating rate Q_{XUV} (Eq. 13) to the locally absorbed XUV radiation

$$Q_{\text{abs}}(r) = \sum_{\lambda} \sigma_{\text{ion},\lambda} n_{\text{H}}(r) F_{\text{XUV},\lambda} \frac{\exp(-\tau_{\lambda}(r))}{1 + \alpha\tau_{\lambda}(r)}. \quad (22)$$

Second, we calculate η_{net} using the net local heating rate $Q_{\text{net}}(r)$ (Eq. 19) divided by $Q_{\text{abs}}(r)$ (e.g. Salz et al. 2016a). A comparison is shown in Fig. 4. The corresponding mean heating efficiencies ($\bar{\eta}_{\text{XUV}}$, $\bar{\eta}_{\text{net}}$) in the atmosphere, obtained by integrating $Q_{\text{XUV}}(r)$ and $Q_{\text{net}}(r)$, respectively, over r and dividing by the stellar XUV flux at the planet's orbit (Table 1) amount to 12% and 3%. The former is in good agreement with detailed studies of the hot Jupiter HD 209458b (Schematovich et al. 2014; Ionov & Schematovich 2015). Note that these heating efficiencies are different quantities than the photoelectron heating efficiency η_{ph} described in Section 2.2.

The effective XUV absorption radius

$$R_{\text{XUV}} = \left(\frac{4\pi \int_{r_0}^{r_1} Q_{\text{XUV}} r^2 dr}{\pi \bar{\eta} F_{\text{XUV}}} \right)^{1/2} \quad (23)$$

(Erkaev et al. 2007, 2015) is about $2.6R_p$ for SF11 and $2.1R_p$ for L14. Using Q_{net} instead of Q_{XUV} in Eq. 23 yields 1.15 (SF11) and $0.78R_p$ (L14), respectively. Note that this radius can be smaller than 1 if Q_{net} is used in Eq. 23 and radiative cooling is very efficient, and/or the mean heating efficiency $\bar{\eta}$ in the denominator is chosen too high. Evaluating the energy-limited mass-loss rate

$$\dot{M}_{\text{el}} = \frac{\pi R_p R_{\text{XUV}}^2 \bar{\eta} F_{\text{XUV}}}{GM_p K} \quad (24)$$

(Erkaev et al. 2007) with these parameters yields $1.5\text{--}3.1 \times 10^{11}$ g s⁻¹ if adopting a typical mean heating efficiency for hot Jupiters of $\bar{\eta} = 15\%$ (e.g. Schematovich et al. 2014) and calculating the tidal enhancement factor K as described in Erkaev et al. (2007). This overestimates the mass-loss rate of HD 189733b by almost an order of magnitude. Adopting the R_{XUV} values obtained with Q_{net} yields $2.1\text{--}6.2 \times 10^{10}$ g s⁻¹, in much better agreement with the hydrodynamic rates. Note that the simple assumption of $R_{\text{XUV}} \sim R_p$ would coincidentally yield mass-loss rates of $3.4\text{--}4.7 \times 10^{10}$ g s⁻¹, similar to the hydrodynamic results, for this specific planet.

3.2. The effect of a flare

HD 189733 is an active star and flares have been detected repeatedly (Pillitteri et al. 2010, 2011, 2014). In Lecavelier des Etangs et al. (2012), an excess absorption of $\sim 14\%$ in Ly α was reported to have occurred during a planetary transit about 8 h after a strong X-ray flare was detected. Here we study if the enhanced XUV flux emitted by such a flare could have increased the planetary mass-loss rate sufficiently to have caused this absorption.

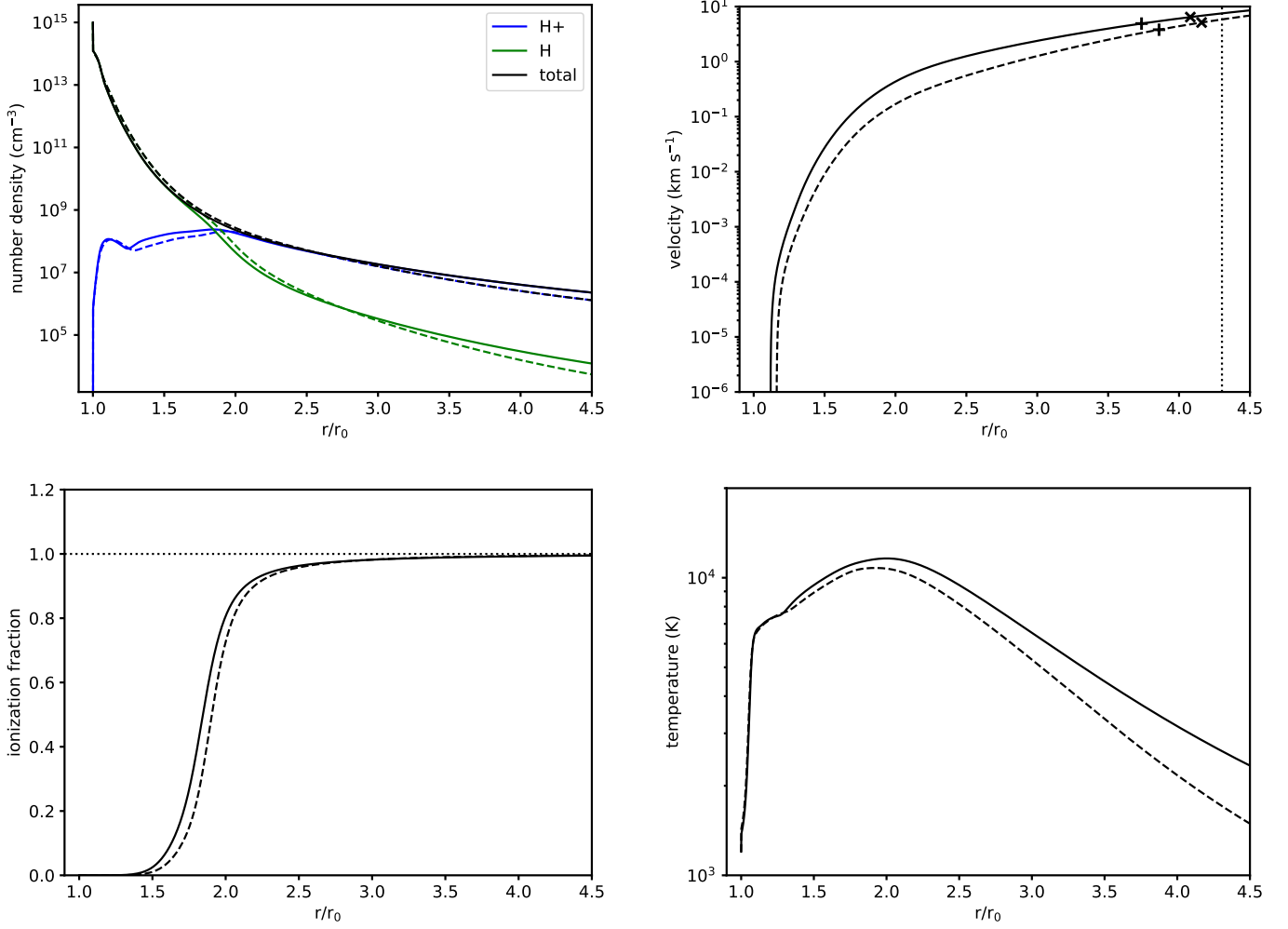


Fig. 2. Atmospheric profiles using the XUV spectra of SF11 (solid) and L14 (dashed). Shown are the number density (total, atomic H, and protons), outflow velocity, temperature and ionization fraction. In the velocity plot, crosses indicate the sonic points and plus signs denote the locations where the outflow velocity exceeds the escape velocity. The dotted line indicates the location of the L1 point.

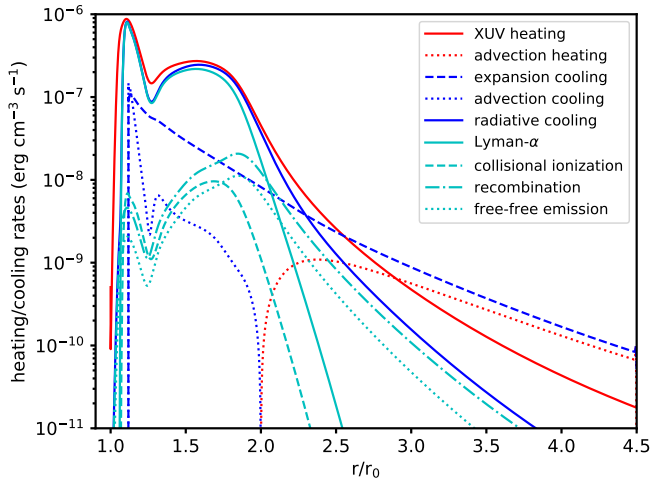


Fig. 3. All heating (red) and cooling (blue) processes included in our model, shown for the SF11 run. The cyan lines show the individual contributions to the radiative cooling rate.

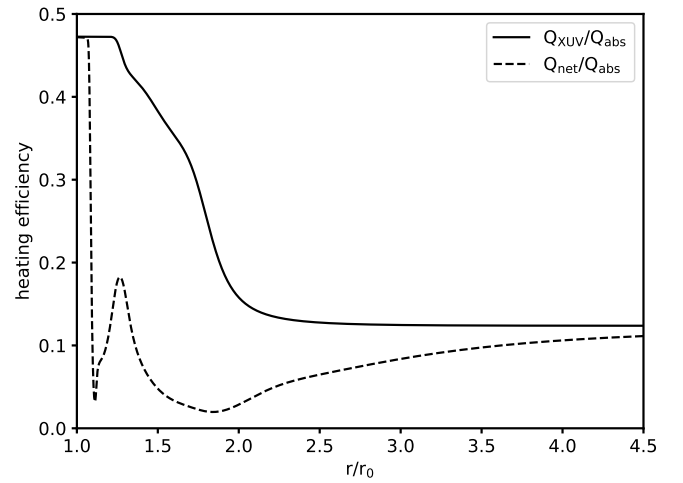


Fig. 4. Heating efficiencies $\eta_{\text{XUV}}(r)$ (solid) and $\eta_{\text{net}}(r)$ (dashed).

The X-ray flux in the 0.3-3 keV band of *Swift*/XRT increased by an average factor of 4 during ~ 27 min, which corresponds to one bin of the temporal resolution of the observations. Together

with the average pre-flare flux of $3.6 \times 10^{-13} \text{ erg cm}^{-2} \text{ s}^{-1}$, this yields an estimated energy of $\sim 8 \times 10^{31} \text{ erg}$ in this bandpass, and is thus a lower limit to the total radiated energy of this flare.

We test the effect of such a flare on the planetary mass-loss rates and the atmospheric profiles. Two cases are considered: firstly, we increase the total XUV flux by the factor of 4 found in X-rays; secondly, we assume that only the X-ray flux increased by a factor of 4 and the EUV flux remained unchanged, since the hot flare plasma could have radiated predominantly at shorter wavelengths, changing the shape of the XUV spectral energy distribution (like solar flares which radiate mostly in X-rays; Chadney et al. 2017). We do not take into account the duration of the flux enhancement, but instead calculate the steady-state solution with these enhanced fluxes. If this solution does not result in a sufficiently high neutral mass-loss rate to explain the observations, a shorter pulse of enhanced radiation would not either. The same conclusions were reached by Chadney et al. (2017), who investigated both the time evolution and steady-state enhancement effects of flares. Note that the true peak flux of the flare is unknown due to the low time resolution of the observations. The duration of the observed flare was approximately 27 min, since there was a significant enhancement in only one temporal bin and the flux in the following bin was comparable to (even slightly lower than) pre-flare levels (see Fig. 4 in Lecavelier des Etangs et al. 2012). Thus, even though the true peak flux could have been higher, its duration cannot have exceeded more than a few minutes, limiting its effect.

Figure 5 shows the flare profiles compared to the results for the average XUV flux for the SF11 spectrum. The profiles for all cases are rather similar. The most apparent differences are the stronger ionization for the XUV flare case and the slightly lower ionization for the X-ray flare case. Also, the temperatures in the upper regions are slightly higher for the flare cases than for the average, but the peak is only slightly increased for the XUV flare. Other than that, the profiles are not strongly altered by exposure to the flare radiation, similar as in the study of Chadney et al. (2017).

The total mass-loss rates are 8.7×10^{10} (X-ray flare) and $1.2 \times 10^{11} \text{ g s}^{-1}$ (XUV flare), higher by factors of 1.6 and 2.2, respectively, compared to the non-flaring state. Our flare-related mass-loss rate enhancements are very similar to the range of 1.8–2.2 found by Chadney et al. (2017). To compare with the modeling of Bourrier & Lecavelier des Etangs (2013), the *neutral* mass-loss rates at $2.95R_p$ (the particle launch radius in their model) are 2.2×10^9 (X-ray flare) and $8.9 \times 10^8 \text{ g s}^{-1}$ (XUV flare), i.e. a factor of two higher (X-ray flare) and by about 10% lower (XUV flare) than in the non-flaring state (10^9 g s^{-1}). This indicates that the enhanced radiation from the flare does not increase the neutral H densities and outflow fluxes sufficiently to account for the observed drastically different atmospheric absorption. More interestingly, although the total mass-loss rate increases for the XUV flare compared to both the non-flaring state and the X-ray flare because of the larger energy input, the *neutral* loss rate is actually smaller due to increased ionization. Note that the neutral outflow rates we obtain are in agreement with those required for the detected absorption ($5 \times 10^8 - 1.5 \times 10^9 \text{ g s}^{-1}$) in the model of Bourrier & Lecavelier des Etangs (2013), but for both flaring and non-flaring states. This indicates that the occurrence of a flare is likely insufficient to produce such strong variability in planetary atmospheric absorption, especially if recalling that the actual flare duration was neglected. The non-detection in 2010 would require a reduction of escape rates by factors 5–20 compared to 2011 (Bourrier & Lecavelier des Etangs 2013). This could only happen if the star was much less active in 2010 com-

pared to our adopted XUV fluxes (reducing the total escape rate), or it was much more active to increase the ionization sufficiently to reduce the *neutral* escape rate despite increasing the total one. From existing observations, the variability in X-rays is about a factor of three (cf. Section 2.4), which is likely not sufficient to account for the variability of atmospheric absorption. However, this contradicts the necessity of similar ionizing fluxes at both epochs in the Bourrier & Lecavelier des Etangs (2013) model. Therefore, other processes may be responsible for, or contribute to, the variable planetary absorption, like variations of the stellar wind. Since strong X-ray flares on the Sun are frequently accompanied by coronal mass ejections (CMEs), we also consider the effect of a possible CME impact in Section 4.3. We note that other upper atmosphere models of this planet find higher ionization (and therefore lower H densities) at this height, yielding much lower neutral loss rates (Guo 2011; Salz et al. 2016a; Chadney et al. 2017), all of which did not obtain such high values at $2.95R_p$. This is mainly related to the smaller number densities assumed at the lower boundary in these studies.

4. MHD flow modeling

4.1. 3D MHD flow model

We use the 3D MHD flow model described in Erkaev et al. (2017) to calculate the plasma flow around HD 189733b (assuming no intrinsic planetary magnetic field) and to obtain the plasma parameters and magnetic field in the region around the planet. This model takes into account radiation and charge-exchange processes acting on the hydrodynamically expanding upper planetary atmosphere penetrating into the stellar wind plasma.

Magnetic field and plasma parameters are determined by the following system of equations for mass, momentum and energy conservation, which are completed by the magnetic induction equation

$$\frac{\partial(\rho V)}{\partial t} + \nabla \cdot \left[\rho V V + \mathbf{I} \left(P + \frac{B^2}{8\pi} \right) - \frac{\mathbf{B}\mathbf{B}}{4\pi} \right] = Q_i V_H - Q_{\text{ex}}(V - V_H) \quad (25)$$

$$\nabla \cdot \mathbf{B} = 0, \quad (26)$$

$$\frac{\partial \rho}{\partial t} + \nabla \cdot (\rho V) = Q_i, \quad (27)$$

$$\frac{\partial \mathbf{B}}{\partial t} - \nabla \times (\mathbf{V} \times \mathbf{B}) = 0, \quad (28)$$

$$\frac{\partial W}{\partial t} + \nabla \cdot \left(\frac{1}{2} \rho V^2 V + \frac{\gamma}{\gamma - 1} P V + \frac{1}{4\pi} \mathbf{B} \times (\mathbf{V} \times \mathbf{B}) \right) = (Q_i + Q_{\text{ex}}) \left(\frac{1}{2} V_H^2 + \frac{3kT_H}{2m_p} \right) - Q_{\text{ex}} \left(\frac{1}{2} V^2 + \frac{3kT}{2m_p} \right), \quad (29)$$

$$W = \frac{1}{2} \rho V^2 + \frac{1}{\gamma - 1} P + \frac{B^2}{8\pi}, \quad (30)$$

where ρ , \mathbf{V} , P , and \mathbf{B} are the mass density, velocity, plasma pressure, and magnetic field of the stellar wind, respectively. The parameter γ is the polytropic index (assumed to be equal to 5/3) and \mathbf{I} is the identity matrix. The parameters V_H and T_H are the velocity and temperature of the escaping atmospheric neutral hydrogen atoms.

The mass conservation equation for ions includes an interaction source term, which is related to photoionization

$$Q_i = \alpha_i N_{\text{H}} m_p \quad (31)$$

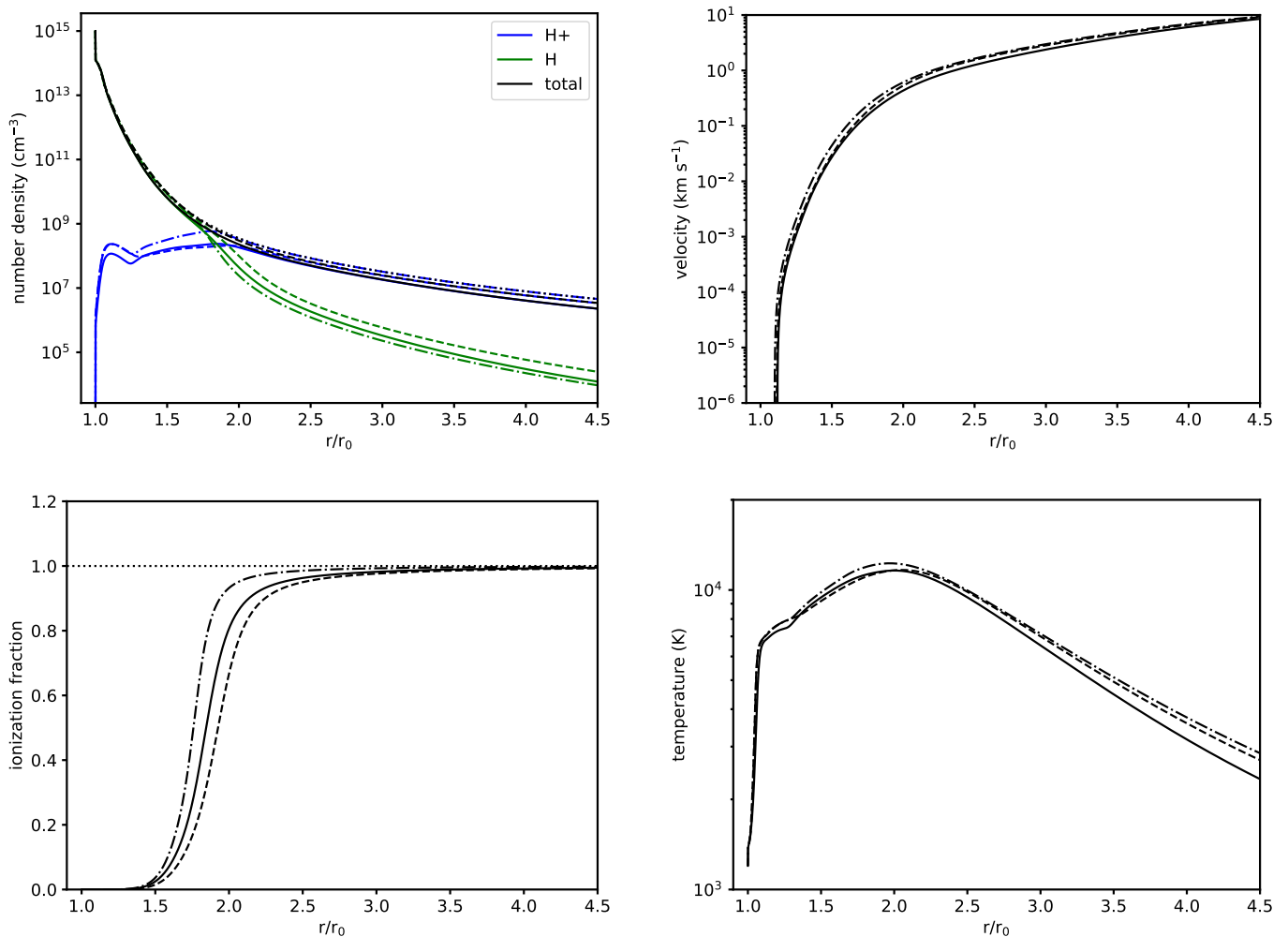


Fig. 5. Atmospheric profiles for average XUV (solid), X-ray flare (dashed), and XUV flare (dash-dotted) based on the SF11 spectrum.

and charge exchange ionization

$$Q_{\text{ex}} = \rho \langle V_{\text{rel}} \rangle N_{\text{H}} \sigma_{\text{ex}} \quad (32)$$

of the hydrogen atoms. Here, N_{H} is the number density of the neutral planetary hydrogen atoms, m_{p} the particle mass, σ_{ex} ($\sim 10^{-15} \text{ cm}^2$) the charge exchange cross section, $\langle V_{\text{rel}} \rangle$ the average relative speed of the stellar wind and atmospheric particles, and $\alpha_i = 5.9 \times 10^{-8} F_{\text{XUV}}$ is the ionization rate proportional to the XUV flux $F_{\text{XUV}} = 1.8 \times 10^4 \text{ erg cm}^{-2} \text{ s}^{-1}$ (cf. Table 2). The numerical scheme for the solution of this system is described in Erkaev et al. (2017).

The neutral hydrogen atoms can be ionized via photoionization or charge exchange processes. However the latter is a dominating ionization mechanism for the atmospheric atoms in the stellar wind region which leads to appearance of low-energy planetary ions and high-energy neutral hydrogen atoms (ENAs) originating from the stellar wind. These newly born ions are immediately accelerated by the local electric field and start to move together with the stellar wind plasma around the planetary obstacle. An acceleration of the picked up ions is accompanied by deceleration of the stellar wind plasma, with conservation of the total momentum.

The streamlined obstacle is considered to be a semi-sphere. The position of the stellar wind stagnation point (R_s) is determined by the pressure balance condition, which means that the

external stellar wind total pressure has to be equal to the momentum flux of the internal ionized atmospheric particles at the boundary. The ratio of the curvature radius of the obstacle to the distance between the stagnation point and the planetary center is taken as 1.3, similar to the value used by Erkaev et al. (2017).

The calculation domain for the MHD stellar wind flow is bounded by the external semi-sphere related to the undisturbed stellar wind region and the internal semi-sphere corresponding to the planetary obstacle. At the outer boundary, we apply the undisturbed stellar wind parameters density, velocity, temperature, and magnetic field. At the obstacle boundary, we assume the normal components of the stellar wind velocity and magnetic field to vanish. Finally we obtain a stationary solution for the stellar wind flow as a result of time relaxation of the non-steady MHD solution. As initial conditions, we set the undisturbed stellar wind parameters in the whole computational domain. The final stationary solution is unique, and it does not depend on the particular initial conditions.

4.2. Stellar wind interaction

Table 3 gives the adopted stellar wind parameters used for the flow model. The mean and maximum values were taken from a 3D stellar wind model (Llama et al. 2013) based on the measured magnetic field map of the star (Fares et al. 2010). Since all

Table 3. Adopted stellar wind parameters at the planet’s orbit.

Parameter	mean	max	CME
N_{sw} (cm^{-3})	4.4×10^5	4.9×10^5	4.4×10^6
V_{sw} (km s^{-1})	326	472	1000
T_{sw} (K)	1.3×10^6	2×10^6	2×10^6
$B_{\text{sw,p}}$ (mG)	44	23	0
$B_{\text{sw,n}}$ (mG)	12	9.5	100
$B_{\text{sw,tot}}$ (mG)	46	25	100
θ_B ($^\circ$)	15	22	90
P_{dsw} (dyn cm^{-2})	7.82×10^{-4}	1.83×10^{-3}	7.36×10^{-2}

wind parameters vary along the orbit depending on longitude, we consider two cases. For the first case (mean) we compute the mean values of number density N_{sw} , velocity V_{sw} , temperature T_{sw} and magnetic field strength along the orbit. We compute both the parallel $B_{\text{sw,p}}$ (parallel to V_{sw}) and normal $B_{\text{sw,n}}$ (normal to V_{sw}) components of its magnitude, as well as the total field strength $B_{\text{sw,tot}}$. The velocity is dominated by the radial component and the magnetic field at the orbit is also dominated largely by the radial (i.e. parallel) field component. The angle θ_B is the angle of the total magnetic field vector and the star-planet line. The second case (maximum) uses the values of the parameters where the ram pressure of the wind along the orbit is maximal. This corresponds to higher values compared to the mean wind (except for B), but not to the maximum values of the individual parameters. We choose this approach because the parameter maxima usually lie at different longitudes (e.g. the maximum velocity corresponds to the minimum density; cf. Fig. D.1). We ignore the velocity of the planetary orbital motion in the following calculations, as the ram pressure of the orbital motion is a factor of 5 smaller than that of the radial wind for the mean wind conditions, and even correspondingly smaller for the other scenarios.

We adopt the hydrodynamic solution of the planetary upper atmosphere obtained with the SF11 XUV spectrum as an input for the MHD flow modeling. Assuming the stellar wind parameters given in Table 3, we apply the 3D MHD flow model to calculate the spatial distribution of the magnetic field and stellar wind parameters in the planetary environment. By solving the non-steady MHD equations, a stationary solution is established as a result of time relaxation. As initial condition, we assume the uniform undisturbed stellar wind flow, which is suddenly stopped at the planetary obstacle. This leads to the appearance of a shock-like wave front propagating outwards from the obstacle. Since we have a super-Alfvénic stellar wind flow, this shock approaches to its stationary position at some distance from the obstacle.

In case of the mean wind, the radial distance to the magnetopause is about $2.6R_p$. Here, the ion and neutral densities of the atmospheric particles are $3.9 \times 10^7 \text{ cm}^{-3}$ and $1.25 \times 10^6 \text{ cm}^{-3}$, respectively, and the temperature is $8.8 \times 10^3 \text{ K}$. In the maximum wind case, the magnetopause position is slightly closer at $2.4R_p$, since the stellar wind dynamic pressure is larger. The corresponding atmospheric ion and neutral densities are $6.1 \times 10^7 \text{ cm}^{-3}$ and $2.9 \times 10^6 \text{ cm}^{-3}$, respectively, and the temperature is $1 \times 10^4 \text{ K}$ (cf. Fig. 2).

Figure 6 shows the spatial distribution of the total pressure P_{tot} (sum of the magnetic and gas pressures) obtained from the numerical MHD model employing the mean stellar wind parameters (see Table 3). Here, the total pressure is normalized to the stellar wind dynamic pressure $P_{\text{dsw}} = N_{\text{sw}} m_p V_{\text{sw}}^2 = 7.8 \times 10^{-5} \text{ Pa}$. The origin of the coordinate system is placed at the planet’s cen-

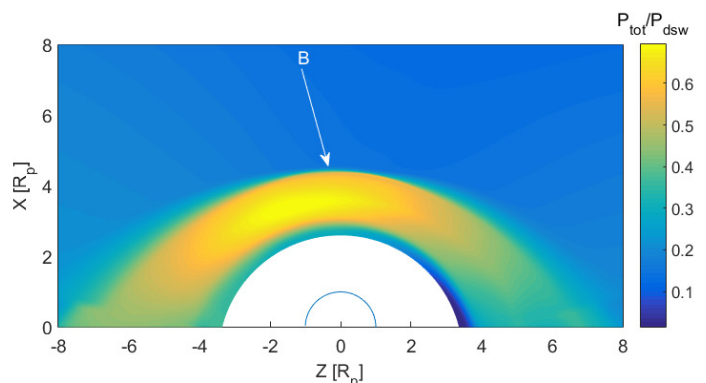


Fig. 6. Cut at $Y=0$ of the simulation showing the distribution of the total pressure (sum of the magnetic and gas pressures) around HD 189733b normalized to the stellar wind dynamic pressure for the mean stellar wind parameters. The white area close to the origin indicates the atmospheric region around the planet, while the semicircle indicates the planetary optical radius. The star is located along the X -axis. The arrow shows the direction of the interplanetary magnetic field.

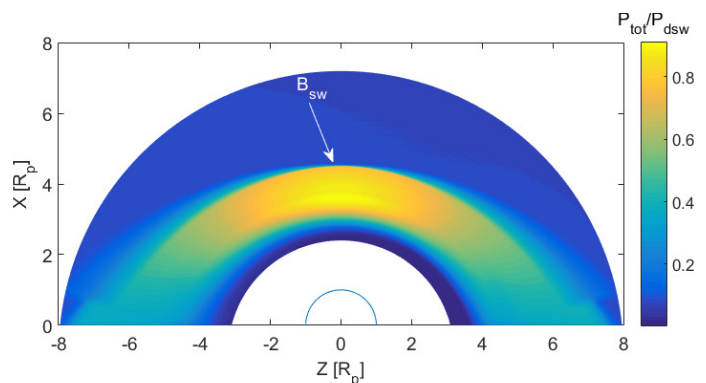


Fig. 7. Same as Fig. 6, but for the maximum stellar wind.

ter, and the star is located along the positive X -axis. The direction of the Z -axis is chosen to have coplanarity between the XZ plane and the interplanetary magnetic field vector \mathbf{B}_{sw} (the arrow in Fig. 6). The white area around the center of the coordinate system indicates the region filled by atmospheric particles exclusively, while the embedded dark blue semi-circle indicates the optical planetary radius R_p . Figure 7 is similar to Fig. 6, but corresponds to the maximum stellar wind parameters. The total pressure in this case is also normalized to the corresponding unperturbed stellar wind dynamic pressure of $P_{\text{dsw}} = 1.8 \times 10^{-4} \text{ Pa}$.

Figure 8 shows the profiles of the ENA and ion densities along the X -axis between the magnetopause and the bow shock (top panel), and also the profiles of the total pressure and temperature (bottom panel) corresponding to the mean stellar wind. The total ion number density has a maximum of about $4 \times 10^4 \text{ cm}^{-3}$ due to charge exchange interaction between the stellar wind plasma and atmospheric neutral atoms which are flowing through the magnetopause. In front of the magnetopause, the ion density and ENA density maxima are about $1.0 \times 10^7 \text{ cm}^{-3}$ and $2.3 \times 10^7 \text{ cm}^{-3}$, respectively. The ENAs form a layer around the magnetopause with a thickness of about $1.3R_p$. Figure 9 is similar to Fig. 8, but corresponds to the maximum stellar wind parameters. In this case, the ion density and ENA density maxima in front of the magnetopause are about $1.13 \times 10^7 \text{ cm}^{-3}$ and $5.6 \times 10^7 \text{ cm}^{-3}$, respectively. The ENA layer thickness around the magnetopause is about $1.2R_p$.

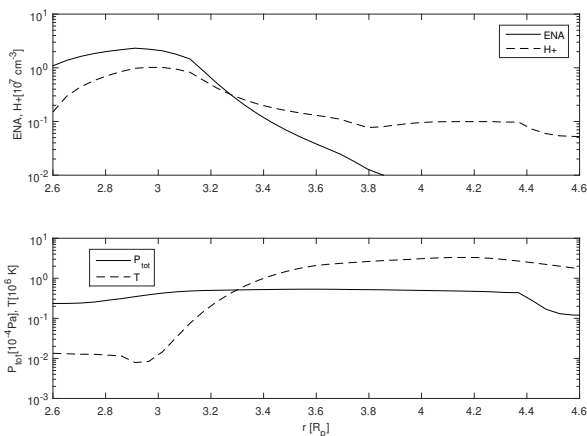


Fig. 8. Profiles of the parameters along the stagnation line from the magnetopause to the bow shock. The top panel shows the ENA and ion densities, the bottom panel the total pressure and temperature for the mean stellar wind conditions.

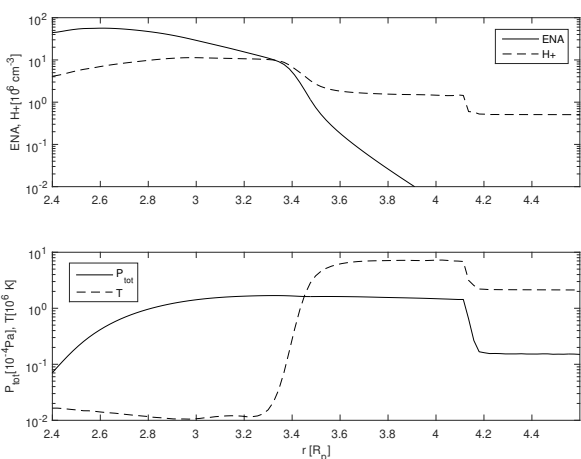


Fig. 9. Same as Fig. 8, but for the maximum stellar wind.

4.3. Impact of a coronal mass ejection

We also consider the case of a stellar CME to study the effect of a potential CME impact. Interaction with a CME could have provided the elevated plasma density levels necessary to produce the observed variability of the planetary Ly α transit signature. On the Sun, large flares are frequently accompanied by CMEs. Empirical models based on flare-CME relationships from the Sun predict high CME occurrence rates for active stars (e.g. Odert et al. 2017, and references therein), because of their high flare rates. The estimated X-ray flare energy of $\sim 8 \times 10^{31}$ erg (cf. Section 3.2) corresponds to a flare that is (almost) always accompanied by a CME on the Sun (Yashiro & Gopalswamy 2009). If the flare was indeed accompanied by a CME, its estimated mass would be in the order of 10^{16} g and its velocity about 1300 km s^{-1} , based on solar scalings (Drake et al. 2013; Odert et al. 2017). We apply an empirical CME prediction model to HD 189733 which calculates CME occurrence rates for Sun-like and cooler main-sequence stars based on their X-ray luminosities L_X (Odert et al. 2017). Adopting $L_X = 1.67 \times 10^{28} \text{ erg s}^{-1}$ (cf. Section 2.4), we obtain about 10–2000 CMEs per day, depending on the power law index of the stellar flare energy distribution, $dN/dE \propto E^{-\alpha}$. We assume $\alpha = 1.5$ – 2.5 , which corresponds to an

observationally determined range typical for the Sun and other stars (Güdel et al. 2003). The mass-loss rate from these CMEs are consistent with observations of stellar mass-loss rates (e.g. Wood 2004, and references therein). However, recent modeling results suggest that CME rates may be lower than estimated from solar scalings due to the stronger magnetic fields on active stars (Alvarado-Gómez et al. 2018), so the obtained numbers are possibly overestimates.

The knowledge on stellar CMEs is still sparse and therefore also the CME activity of HD 189733 is not constrained by observations. One method to detect stellar CMEs is from transient blue-wing asymmetries or blue-shifted extra-emissions or absorptions (depending on geometry) in Balmer lines, which probe the (partly) neutral prominence material embedded in the ejecting CME core (e.g. Leitzinger et al. 2014, and references therein). We analyzed archival optical spectroscopic observations of HD 189733 (430 Stokes I spectra from PolarBase; Petit et al. 2014) as described in Leitzinger et al. (2020). The total on-source time of the spectra is about 122 h and the observations span the years 2006–2015. We find no signatures of CMEs in the Balmer lines. With this non-detection we estimate <0.6 observable CMEs per day (95% confidence). It is important to correct for the expected H α emission and geometrical constraints, since not all occurring CMEs are necessarily observable with a given method. We use a model which takes into account the expected maximum possible CME core emission in Balmer lines and geometrical constraints, considering the total on-source time and average signal-to-noise ratio of the spectra (Odert et al. 2019). It predicts that $\leq 1\%$ of the occurring CMEs would be observable in H α on HD 189733 for the given observational parameters. The estimated maximum observable CME rates are comparable to the upper limit from the analyzed observations, indicating that much longer observing times and/or higher quality of the spectra would be required to determine the CME rate of this star with this method. Note that none of the analyzed H α observations were taken during the time of the studied flare and transit in 2011. Due to this non-detection, we have to rely on reasonable extrapolations from the Sun to estimate plausible CME parameters for this star.

We assume a velocity of 1000 km s^{-1} which is commonly found for energetic CMEs already close to the Sun (Yashiro et al. 2004), and which is also similar to the CME velocity derived above from the estimated flare energy. For the density we use an enhancement factor of 10 compared to the mean wind, which is also common for solar CMEs at separations of a few solar radii (Schwenn et al. 2006). Note that we cannot use solar CME density profiles as e.g. in Khodachenko et al. (2007), because the modeled stellar wind densities at HD 189733b’s orbit are already higher than the solar CME densities given in Khodachenko et al. (2007) at these orbital distances. Due to the lack of knowledge on stellar CME temperatures, we simply adopt the maximum wind value. For the magnetic field we use 100 mG, similar to values at around $10R_\odot$ from the Sun (Patsourakos & Georgoulis 2016). The angle is assumed to be 90° , corresponding to the geometry of a centrally impacting ejected flux rope, as commonly observed in solar CMEs. With the assumed velocity, a CME would need about 1 h to reach the planet’s orbit. The typical duration of solar CMEs at a few solar radii is about 8 h (Lara et al. 2004). This means that if a CME occurred simultaneously with the flare, the planet may have still been exposed to a plasma environment dominated by the CME. The adopted CME parameters are given in Table 3.

Figure 10 shows the spatial distribution of the total pressure obtained with the MHD flow model for the adopted CME param-

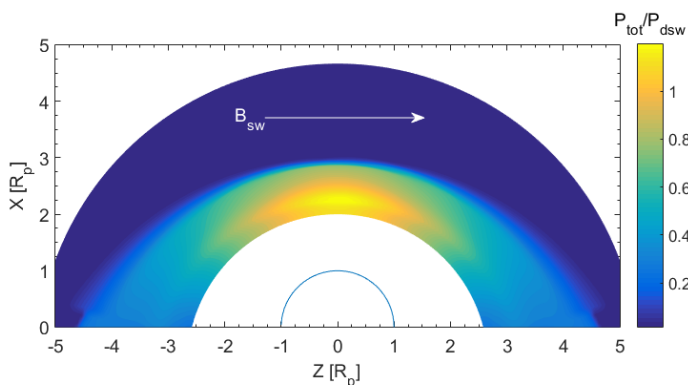


Fig. 10. Same as Fig. 6, but for the CME conditions.

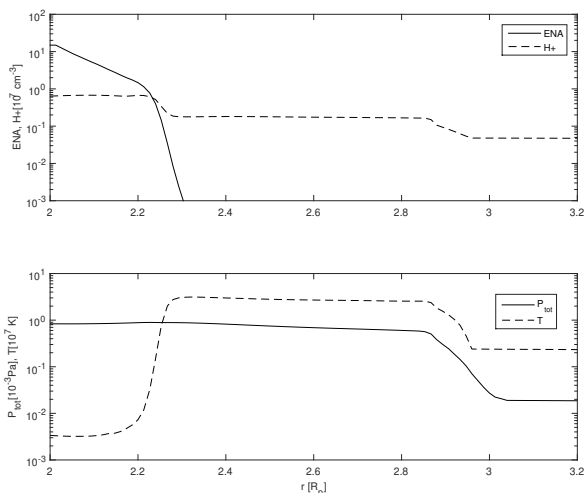


Fig. 11. Same as Fig. 8, but for the CME conditions.

eters (Table 3). In this case, the magnetopause is located closer to the planet compared to both wind cases because of the higher dynamic pressure, at a distance of $\sim 2R_p$. The corresponding atmospheric ion and neutral densities are about $1.8 \times 10^8 \text{ cm}^{-3}$ and $4.5 \times 10^7 \text{ cm}^{-3}$, respectively, and the temperature is $1.16 \times 10^4 \text{ K}$ (cf. Fig. 2). The total pressure is again normalized to the CME dynamic pressure of $P_{\text{dsw}} = 7.35 \times 10^{-3} \text{ Pa}$. The ion density and ENA density maxima in front of the magnetopause (Fig. 11) are about $0.67 \times 10^7 \text{ cm}^{-3}$ and $1.5 \times 10^8 \text{ cm}^{-3}$, respectively. The ENA layer is much thinner in the CME case, its thickness is about $0.25R_p$.

Table 4 summarizes the results of the stellar wind interaction modeling. It compares the stand-off distances, the thickness of the ENA layer, and the maximum number densities of ENAs and ions in front of the magnetopause. Stronger winds or CMEs confine the planetary atmosphere to smaller regions because of the higher ram pressures. Higher stellar wind ram pressures also lead to more compressed, thinner ENA layers, but with higher maximum densities.

5. Modeling the Ly α absorption signature

To calculate the transmissivity in the Ly α line, we assume that a hydrogen cloud surrounding the planet consists of two parts: a spherically symmetric lower atmosphere corresponding to the 1D atmospheric profile and an upper exospheric part consisting

Table 4. Stand-off distances, ENA layer thickness, and maximum number densities of ENAs and ions in front of the magnetopause.

Wind	stand-off distance (R_p)	ENA layer thickness (R_p)	ENA density maximum (cm^{-3})	ion density maximum (cm^{-3})
mean	2.6	1.3	2.3×10^7	1.0×10^7
max	2.4	1.2	5.6×10^7	1.13×10^7
CME	2	0.25	1.5×10^8	0.67×10^7

of energetic neutral atoms (ENAs) calculated by the 3D MHD model. We consider one atmospheric profile (Fig. 2) and three different stellar wind cases: the mean wind, the maximum wind, and the CME case (Table 3). After a hydrogen cloud is simulated (Figs. 6, 7, 10) and by knowing the positions and velocities of all hydrogen particles, we compute how these atoms attenuate the stellar Ly α radiation by using a post-processing software written in the Python programming language. To compute the transmissivity along the line-of-sight we follow the approach of Semelin et al. (2007). The post-processing tool has been described in detail in Kislyakova et al. (2014). Here we repeat the main features of it.

Only neutral hydrogen atoms absorb in the Ly α line. One has to take into account spectral line broadening. Real spectral lines are subject to several broadening mechanisms: *i*) natural broadening; *ii*) collisional broadening; *iii*) Doppler or thermal broadening. The ‘‘natural line width’’ is a result of quantum effects and arises due to the finite lifetime of an atom in a definite energy state. A photon emitted in a transition from this level to the ground state will have a range of possible frequencies $\Delta f \sim \Delta E / \hbar \sim 1 / \Delta t$, which can be approximated by a Lorentzian profile. Collisional broadening is caused by the collisions randomizing the phase of the emitted radiation. This effect can become very important in a dense environment, yet above the exobase it does not play a role and is important only in the lower parts of the atmosphere, therefore, we do not take it into account.

The third type of broadening, which plays a significant role in the upper atmosphere of a hot exoplanet, is thermal broadening, which arises because the frequency of the absorption is shifted due to the Doppler effect. In the considered cases, an analytical solution for the absorption profile cannot be obtained, since it is not only thermal atoms that contribute to the broadening, but also ENAs. For this reason, we can not use a Voigt profile (which can be used for a pure Maxwellian distribution). We calculate the natural broadening for all atoms and bin it by velocity, which automatically gives us the Doppler broadening for a particular velocity distribution.

To compute the transmissivity along the line-of-sight we follow the approach of Semelin et al. (2007) and Kislyakova et al. (2014). We use a Cartesian coordinate system with the x -axis pointing towards the star, the y -axis directed antiparallel to the planetary motion, and the z -axis completing the right-handed coordinate system. We calculate the relation between the observed intensity I and the source intensity I_0 as a function of frequency f of the stellar spectrum in the yz -plane by dividing the computational domain into a grid with N_c cells. For each cell in the grid along lines-of-sight in front of the star ($y^2 + z^2 < R_*^2$), the velocity spectrum of all hydrogen atoms in the column along the x -axis can be calculated. We account for the planetary inclination by shifting the cloud by $z = a \cos i = 3.67 \times 10^{10} \text{ cm}$ relative to the center of the stellar disc at mid transit. Then the transmissivity can be averaged over all columns in the yz -grid except those par-

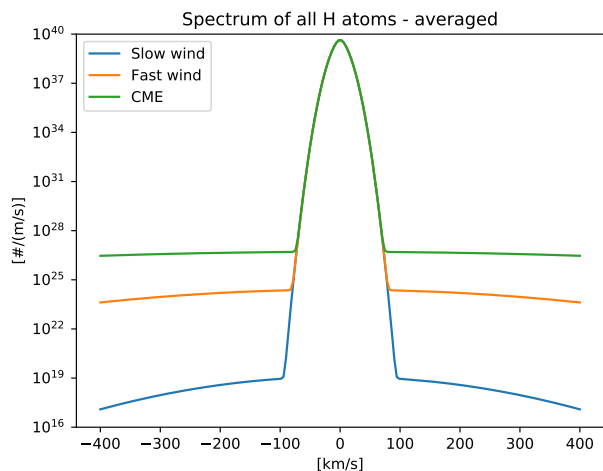


Fig. 12. Velocity spectra of neutral H atoms for the atmosphere of HD 189733b for mean (blue), maximum (orange), and CME conditions (green). The main peak presents the atmospheric neutrals, the low and wide wings are the ENAs with different bulk velocities and high temperatures.

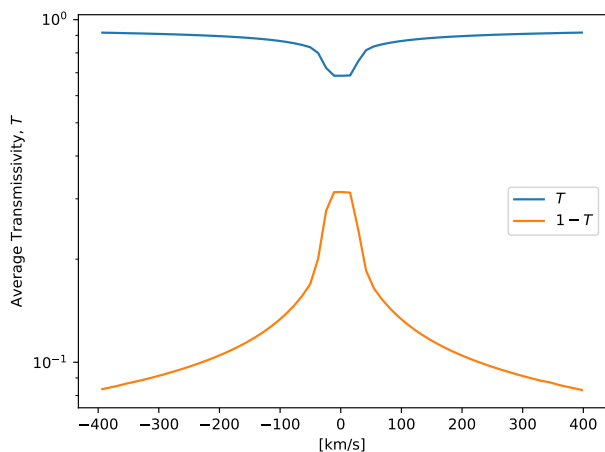


Fig. 13. Calculated transmissivity (blue) and corresponding absorption (orange) in the Ly α line as a function of velocity. The results for the mean wind parameters are shown, but the other two cases produce indistinguishable results due to the dominating contribution of atmospheric broadening.

ticles which fall outside the projected limb of the star or inside the planetary disc.

We use the frequency-dependent cross-section, which depends on the normalized velocity spectrum, the Ly α resonance wavelength and the natural absorption cross-section in the rest frame of the scattered hydrogen atom (Peebles 1993). For lines-of-sight in front of the planet $(y - y_p)^2 + (z - z_p)^2 < R_p^2$, where (y_p, z_p) is the planet center position, we set zero transmissivity.

To account for the contribution of the lower atmosphere, a Maxwellian velocity spectrum corresponding to a hydrogen gas with a specified column density and temperature is added to all pixels up to the outer extent of the atmosphere, according to the atmospheric profile calculated with the 1D HD code. In a similar way, to account for the ENAs we add a Maxwellian spectrum corresponding to their temperatures with the central velocity located at their bulk velocity, which is different depending on their

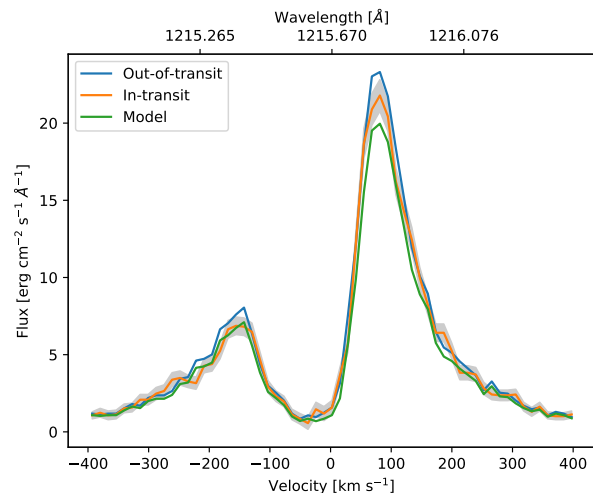


Fig. 14. Modeled absorption of HD 189733b compared to the out-of-transit observation of the planet for the 2011 data (Lecavelier des Etangs et al. 2012). The blue line shows the observed out-of-transit Ly α profile of HD 189733. The green line shows the modeled in-transit absorption. The orange line shows the in-transit absorption observed in September 2011. The shaded region surrounding the orange line shows the observational errors. One can see that our modeled spectrum reproduces well the observed profile, also in its red part, and is mostly within the error boundaries. Mean wind conditions were adopted, but the other cases produce identical results. The region between $-40 \dots +40 \text{ km s}^{-1}$ was affected by geocoronal emission in 2011 and should be ignored (Bourrier & Lecavelier des Etangs 2013).

position relative to the magnetopause boundary. Due to the formation of a bow shock, ENAs are generated from decelerated stellar wind ions and have thus a speed much slower than that of the stellar wind, but on the same time obtain a very high temperature, manifesting in a very broad spectrum spanning from very low up to very high velocities along the x -axis.

Figure 12 shows the velocity spectra of all neutral H atoms along the line-of-sight, including atmospheric particles (the main central peak on the plot) and the ENA population (seen as the wide “wings” on both sides of the velocity spectra) for all three considered cases. Positive velocities and negative velocities correspond to atoms flying towards and away from the star, respectively. The velocity spectrum of an atomic cloud can then be converted to frequencies via the relation $f = f_0 + v_x/\lambda_0$ with $f_0 = c/\lambda_0$, $\lambda_0 = 1215.65\text{\AA}$, and where c is the speed of light. As one can see, ENAs form very wide wings around the central atmospheric peak. Different initial values for temperature, density, and velocity of the stellar wind influence the height and the flatness of the wings. However, one can see that all three cases produce very flat wings, which is due to a sharp temperature increase and wind deceleration near the planetary boundary.

Figure 13 shows the calculated average transmissivity and absorption for the mean wind spectrum shown in Fig. 12. Despite differences in the velocity spectra in the ENA part, the transmissivity spectra **are indistinguishable**, so we do not show the other cases. This is due to the fact that the contribution from the ENAs produces very flat and low spectra, with the amount of particles in a given velocity bin not high enough to produce any significant contribution. Therefore, the absorption is mostly determined by the atmospheric broadening from the dense central peak, which is identical in all three cases, because we used the same atmospheric profile.

Finally, Fig. 14 compares the calculated absorption to the Ly α in-transit observations of HD 189733b from 2011. It was obtained by multiplying the out-of-transit spectrum (blue) by the transmissivity (Fig. 13). This simple method may generate a bias if applied to the analyzed observations because of the combination of the broad line spread function of STIS and the ISM absorption, but this is limited to the region close to the line core where the ISM absorption is saturated, but should not affect the line wings where the planetary absorption is detected. In general, there is a good agreement between the calculated and observed spectra **although the absorption predicted by our model is slightly larger. Outside of the geocoronal emission region, the modeled blue-wing ($-400 \dots -40 \text{ km s}^{-1}$) absorption is 10.9%, 1.7 σ larger than the observed value ($6.8 \pm 2.4\%$); for the red wing ($-40 \dots 400 \text{ km s}^{-1}$), we obtain with 12.9% too much absorption by 5.5 σ (observed: $4.5 \pm 1.5\%$). This means that the model with our default parameters predicts slightly too large neutral densities. If scaling the modeled absorption profile to match the blue-wing absorption, the red-wing absorption would be within 3 σ of the observations.** As one could expect from Fig. 13, **we find insignificant differences of the absorption for the different wind scenarios due to the negligible contribution of ENAs in our model.** This conclusion contradicts the one by Kislyakova et al. (2014), who were able to reproduce the Ly α observations of HD 209458b only assuming a specific wind configuration. This contradiction can be easily explained by the fact that the Direct Simulation Monte Carlo model by Kislyakova et al. (2014) did not account for the deceleration and temperature increase of the ENAs near the planetary obstacle. For this reason, their results only accounted for a Maxwellian spectrum according to the initial density, temperature, and velocity distribution. On the contrary, our results represent a better approximation of the wind properties near the planet, and show that different stellar wind conditions produce similar Ly α signatures. Differences to previous studies are discussed in more detail in Section 6.3.

One should keep in mind that we did not account for the compression and additional ionization of the atmosphere by the stronger stellar wind, therefore, our results still present an approximation, even though they present a significant improvement in comparison to earlier works by Holmström et al. (2008); Kislyakova et al. (2014).

6. Discussion

6.1. Comparison with other hydrodynamic models

As described above, our simulations yield a total mass-loss rate of $\dot{M} = 2.5\text{--}5.4 \times 10^{10} \text{ g s}^{-1}$, depending on the adopted XUV spectrum. Previous studies of this planet found $\dot{M} = 4.8 \times 10^{10}\text{--}2 \times 10^{11} \text{ g s}^{-1}$ for $F_{\text{XUV}} = 2 \times 10^4\text{--}10^5 \text{ erg cm}^{-2} \text{ s}^{-1}$ (Guo 2011), $\dot{M} = 4.5 \times 10^{11}\text{--}9 \times 10^{11} \text{ g s}^{-1}$ for $F_{\text{XUV}} = 24778 \text{ erg cm}^{-2} \text{ s}^{-1}$ (but different spectral energy distributions; Guo & Ben-Jaffel 2016), and $\dot{M} = 1.64 \times 10^{10} \text{ g s}^{-1}$ for $F_{\text{XUV}} = 20893 \text{ erg cm}^{-2} \text{ s}^{-1}$ (Salz et al. 2016a)³. Despite using similar XUV fluxes, the model of Salz et al. (2016a) yields a mass-loss rate lower by more than an order of magnitude compared to the other studies (Guo 2011; Guo & Ben-Jaffel 2016), which is likely because not all relevant radiative cooling processes were included in the latter models, leading to an overestimate of the escape rate. Our mass-loss rates are up to a factor of 3

³ Their given value of $4.1 \times 10^9 \text{ g s}^{-1}$ corresponds to 1/4 of the isotropic mass-loss rate.

higher than Salz et al. (2016a). Estimating the spectral shape with a ratio of fluxes like in Guo & Ben-Jaffel (2016) we find $\beta = F_{50\text{--}400\text{Å}}/F_{50\text{--}900\text{Å}} \sim F_{0\text{--}400\text{Å}}/F_{0\text{--}912\text{Å}} \sim 0.8$ for both spectra, corresponding to a mass-loss rate of $\sim 9 \times 10^{11} \text{ g s}^{-1}$ in their model (see their Fig. 13), which is a factor of 15 higher than our results.

The atmospheric profiles are compared in Fig. 15. For Guo (2011) we adopted their results for $F_{\text{XUV}} = 2 \times 10^4 \text{ erg cm}^{-2} \text{ s}^{-1}$ (their Fig. 3). One can see that our model yields lower velocities, but higher densities throughout the computational domain. Moreover, ionization occurs at a greater height compared to their results. This could partly be related to the much lower densities adopted at R_p in the other studies, as well as different XUV spectra. The temperature maximum is comparable to Salz et al. (2016a), but it is located further out at about $2R_p$ instead of $1.5R_p$.

The main differences between the discussed models are: gray atmosphere approximation, no molecules, only H, only Ly α cooling in Guo (2011); XUV spectra, molecules, H+He, but only H $_3^+$ cooling in Guo & Ben-Jaffel (2016); XUV spectra, no molecules, H+He, all atomic radiative cooling processes in Salz et al. (2016a); XUV spectra, no molecules, only H, all atomic cooling processes in the present study. In addition, there are some differences in the adopted star/planet parameters and lower boundary conditions, as well as usage of different solution methods of the hydrodynamic equations. Therefore, some differences in the mass-loss rates and atmospheric profiles are to be expected. We find the best qualitative agreement with Salz et al. (2016b) in that HD 189733b is an intermediate case between planets with high escape rates and stable planets in radiative equilibrium.

6.2. Neglected processes

There are several processes which are not considered in our present model that may have an impact on the planetary escape rates and thus the modeled transit absorption. First, usage of a 1D hydrodynamic code for the upper atmosphere limits the validity of the results to a region well within the Roche lobe. The average Roche lobe radius of HD 189733b is $\sim 3.1R_p$ (Eggleton 1983), smaller than the distance to the L1 point (cf. Section 2.3). Close to and beyond the Roche lobe, the gas dynamics are dominated by 3D effects (e.g. Bisikalo et al. 2013). However, we find that even for mean stellar wind conditions the pressure balance distance is at about $2.6R_p$, i.e. well within the Roche lobe, which justifies using the 1D results for the atmosphere up to this point. However, we note that the sonic point is reached close to the L1 point above $4R_p$, which means that the dynamic pressure of the stellar wind at this point is larger than that of the planetary outflow. This means we could be overestimating the escape rates because the stellar wind may confine the planetary mass-loss. However, it is possible that the confinement on the dayside is (partly) compensated by a stronger outflow on the nightside (Murray-Clay et al. 2009; Shaikhislamov et al. 2016). On the other hand, the absorbed XUV energy could also be radiated away by Ly α and free-free cooling due to the enhanced temperatures, which would lead to a reduction of the escape rates (Salz et al. 2016a). Self-consistent modeling of planetary-stellar wind interaction would require a multi-dimensional multi-fluid model.

Due to the strong ionization of hot Jupiter atmospheres, an intrinsic planetary magnetic field may lead to a reduction of the escape rate (Owen & Adams 2014; Trammell et al. 2014; Khodachenko et al. 2015). It is unknown if HD 189733b possesses

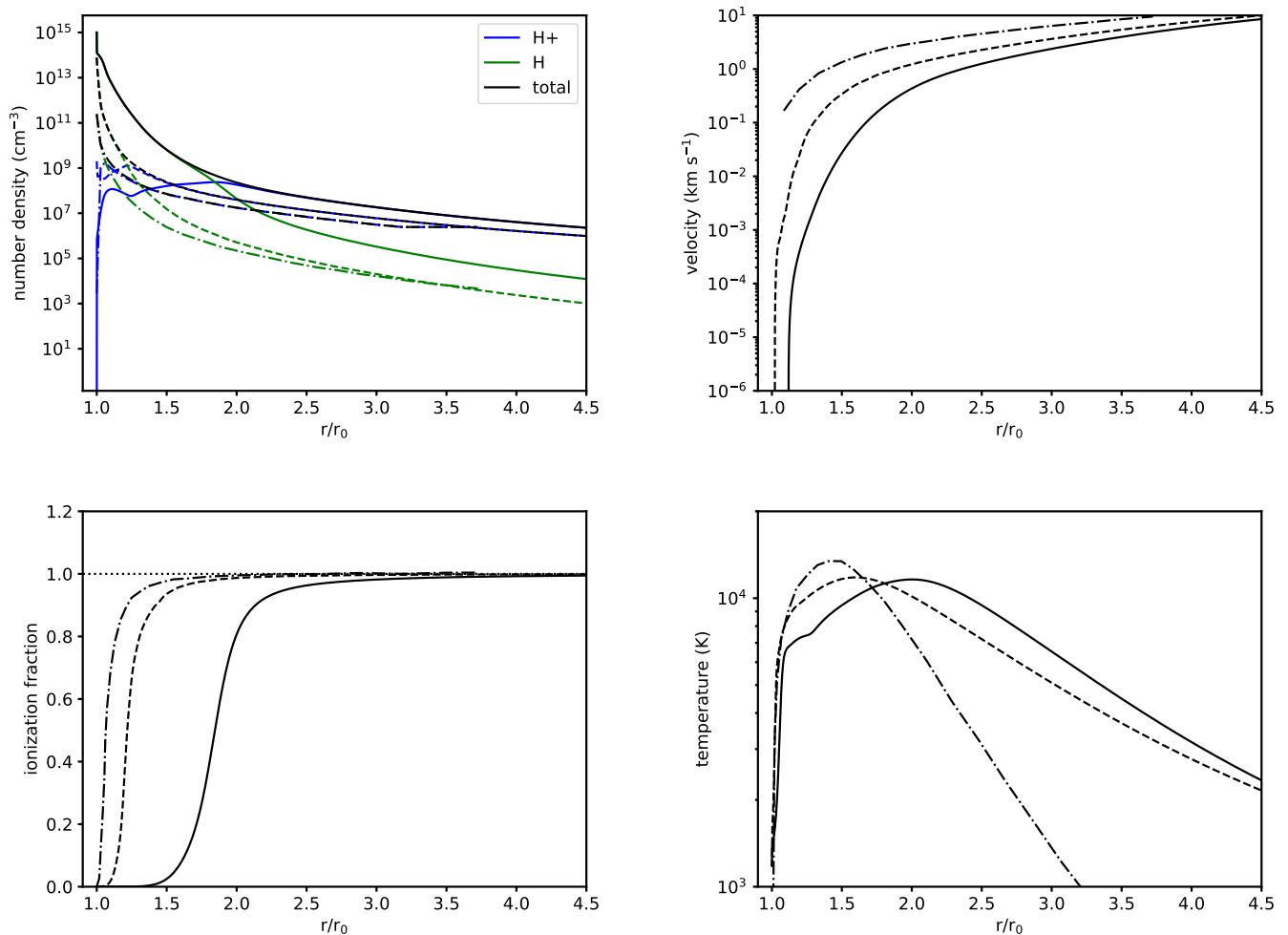


Fig. 15. Atmospheric profiles for the SF11 run (solid) compared with previous model results of (Guo 2011) (dash-dotted) and (Salz et al. 2016a) (dashed).

an intrinsic magnetic field strong enough to affect its mass-loss. However, we do consider the generation of an induced magnetic field at the obstacle (magnetic barrier) in our MHD model (Erkaev et al. 2017). An intrinsic planetary magnetic field may push the pressure balance distance with the stellar wind further out.

We include only hydrogen atoms and protons in our simulations. Neglecting H_2 and its related ions is justified for this planet because its presence is confined to a very small region close to the optical radius (see Guo & Ben-Jaffel 2016, and Section C). This also means that cooling by H_3^+ is not important here due to its small number density. However, helium is likely to be present in the atmosphere with cosmic abundances. Salz et al. (2016a) compared hydrodynamic simulations with and without including He and found mass-loss rates lower by a factor of two in the former case.

6.3. Comparison with previous transit signature modeling

Bourrier & Lecavelier des Etangs (2013) describe the details of the 3D particle model which they use to explain the Ly α observations of HD 189733b (Lecavelier des Etangs et al. 2012). It depends on the planetary mass-loss rate of neutral H, ionizing flux (limiting the lifetime of H atoms), and stellar wind param-

eters at the orbit (V_{sw} , N_{sw} , T_{sw}). It includes radiation pressure, planet/star gravities, charge exchange with stellar wind protons, and self-shielding of stellar photons and stellar wind protons by the H cloud. They find best fits to the 2011 observations for $V_{\text{sw}} = 200 \text{ km s}^{-1}$, $T_{\text{sw}} = 3 \times 10^4 \text{ K}$, $N_{\text{sw}} = 10^3 - 3 \times 10^5 \text{ cm}^{-3}$, an ionizing flux 10 times solar, and neutral H escape rates of $5 \times 10^8 - 1.5 \times 10^9 \text{ g s}^{-1}$. Compared to 2010, for fixed wind parameters the H escape rates would need to be 5-20 times lower; for fixed ionizing flux and escape rate, the stellar wind proton densities must be about a factor of 10 lower. This indicates that the 2011 observations can be explained with a higher H escape rate (but not much higher ionizing flux) or a denser wind compared to 2010. Lecavelier des Etangs et al. (2012) suggested that these discrepant observations could be due to a flare which occurred ~ 8 h prior to the transit in 2011.

The model of Bourrier & Lecavelier des Etangs (2013) may explain the observed Ly α absorption in 2011 if a neutral H mass-loss rate in the order of 10^9 g s^{-1} at $2.95 R_p$ (the lower boundary of their model) occurs. Our H mass-loss rate at this altitude is comparable to this requirement, but similar for normal and flaring cases (see Section 3.2), even if ignoring the limited duration of the enhanced XUV fluxes. Hence, our neutral loss rates are consistent with their model for the 2011 observations, but they cannot explain the non-detection in 2010 because the XUV

fluxes must have been very different. Either the fluxes were much lower, reducing the total mass-loss rate, or much higher, reducing the neutral H density due to enhanced ionization. This contradicts the necessity of similar ionizing fluxes at both epochs (Bourrier & Lecavelier des Etangs 2013). Test simulations with significantly enhanced XUV fluxes show that even an increase by a factor of 1000 only decreases the neutral H mass-loss rate by a factor of three. For lower XUV fluxes, the total mass-loss rate decreases, but the neutral H mass-loss rate increases relative to our results (e.g. about a factor of two larger for a factor of five lower XUV). However, we stress that other hydrodynamic models of this planet find higher ionization (and therefore lower H densities) at $2.95 R_p$, yielding much lower neutral loss rates (Guo 2011; Salz et al. 2016a; Chadney et al. 2017). We find that this is mainly related to the lower number densities assumed at the lower boundary in these studies. If we run our model with lower n_0 values, we also obtain too low neutral densities at $2.95 R_p$ compared to those required in Bourrier & Lecavelier des Etangs (2013). This indicates that the neutral density at a given altitude does not just depend on the irradiating stellar XUV flux, but strongly depends on n_0 , stronger than the total mass-loss rate. Higher values of n_0 shift the neutral-ion transition to larger heights. However, we find that lowering n_0 results in incomplete absorption of the XUV radiation in the computational domain, which makes the resulting mass-loss rates strongly dependent on the assumed n_0 .

One may argue that if the true value of n_0 would indeed be much lower than our assumptions, the absorption signal from the planetary atmosphere could be much weaker than what our results show and not compatible with the 2011 observations. However, it is unlikely that n_0 can be much smaller, because too much ionizing radiation would then reach layers close to the optical radius or even below, inconsistent with the observed value of the optical radius. The only possibility that the upper atmosphere could absorb most of the ionizing radiation above R_p despite a lower H density could be efficient absorption by non-hydrogen species (such as the absorption of X-rays by metals). If this effect could be strong enough for reasonable atmospheric metallicities should be addressed in future studies.

The other possible explanation for the transit variability in the Bourrier & Lecavelier des Etangs (2013) model is a higher stellar wind density in 2011 by a factor of about 10. Our results are not consistent with this picture, as we find a negligible influence of the stellar wind on the absorption, even in case of a putative CME impact which may have been related to the flare. The absorption in our model is completely dominated by the contribution from the parts of the planetary atmosphere below the pressure balance distance (Section 5). We tested the effect of adopting stellar wind parameters more similar to the best fitting model of Bourrier & Lecavelier des Etangs (2013) in our MHD model, namely $V_{sw} = 200 \text{ km s}^{-1}$, $T_{sw} = 3 \times 10^4 \text{ K}$, $N_{sw} = 10^6 \text{ cm}^{-3}$, and keeping the magnetic field parameters of our mean wind case. We find that the maximum ENA density is much smaller than in the cases from Table 3, and that their bulk speed is small compared to the local thermal speed of the stellar wind. Therefore, such a wind does not produce a tail and a localized blue-shifted absorption signature in our model.

Previous modeling approaches employed Monte Carlo particle codes to model the generation and distribution of ENAs around exoplanets (Holmström et al. 2008; Bourrier & Lecavelier des Etangs 2013; Kislyakova et al. 2014). ENAs generated in such models by charge exchange of neutral planetary atoms with the stellar wind have a velocity distribution peaked at the stellar wind speed. After formation, ENAs are generally not cou-

pled to the plasma flow due to lack of collisions; their motion is controlled by gravitational, centrifugal and Coriolis forces, as well as radiation pressure (e.g. Kislyakova et al. 2014). For HD 189733b, the situation is different. The high densities in the circumplanetary environment lead to an efficient coupling of ENAs and ions by collisions⁴. This justifies modeling ENAs in the HD 189733 system with our MHD code. In our model, the ENAs are generated inside the bow shock. These ENAs have thus velocities much smaller than that of the stellar wind because they are formed from decelerated wind ions. This leads to ENA velocity spectra which peak at small velocities (Fig. 12). Due to strong ionization by the intense XUV flux, the upper planetary atmosphere is almost completely ionized, so generation of additional ENAs outside the bow shock (which would have velocities comparable to the stellar wind) can likely be neglected here due to the very small available amount of planetary neutrals.

As described in Section 6.1, Guo & Ben-Jaffel (2016) used a hydrodynamic upper atmosphere model similar to ours in combination with different spectral energy distributions of the stellar XUV radiation. They are able to reproduce the 2011 observations with a spectral shape $\beta = 0.76$, which is very similar to our adopted Sanz-Forcada et al. 2011 spectrum ($\beta = 0.82$) that also reproduces the transit absorption. The non-detection in 2010 would require a spectral shape of $\beta = 0.38$. Our results are consistent with theirs in that the 2011 observations can be reproduced solely considering the planetary atmosphere, ENAs being negligible. However, due to the difficulties in observing the EUV emission of stars it is unknown if such strong temporal changes in spectral shape would be possible while leaving the total emission almost unchanged.

6.4. Effects of flares on the upper atmosphere

As described before, with our adopted mean XUV spectrum we can reproduce the transit observations from 2011. Thus, no anomalous stellar emission like a flare is needed to produce the absorption. As discussed in Section 3.2, the X-ray flare observed 8 h before the planetary transit in 2011 was unlikely able to induce any measurable difference in planetary absorption. Stellar emissions increased by a factor of four in X-rays/XUV raise the total mass-loss rates by 60/120%, respectively. In the latter case, however, the *neutral* mass-loss rates drop because of increased ionization. Using a realistic time evolution of a flare and not just a constant elevation of the irradiation would make the effects even smaller. Our findings are in agreement with Chadney et al. (2017) who studied the effect of flares on the upper atmospheres of close-in exoplanets. They also found that a flare is likely not capable of producing the strong modulation of the transit absorption as seen in HD 189733b, but suggest that a stellar proton event could cause such differences.

6.5. Stellar activity effects on the Ly α transit absorption

Stellar activity can also affect the study of Ly α transit absorption in other ways than a modulation of the planet's atmosphere. To obtain the amount of absorption during the transit, the in-transit spectrum is usually compared to an out-of transit spectrum. This can cause difficulties in case of an active star because of two main reasons. First, the surface of a star may not be homogeneous due to the presence of active regions. Second, the star may be variable on time scales comparable to the planetary transit, so

⁴ Taking $n \gtrsim N_{sw}$, $\sigma_{col} \sim 10^{-15} \text{ cm}^2$ and $X \sim R_p$ yields a Knudsen number $Kn < 1$ in the modeling domain.

that the stellar background emission during the transit could be different from the stellar spectrum recorded some time before the transit.

The first effect was studied in Llama & Shkolnik (2015), who simulated hot Jupiter transits over solar X-ray, EUV, FUV, and optical images. Both occulted and unocculted active regions can modify the obtained absorption. It also depends if the active regions are brighter or darker than the inactive stellar disk in a given wavelength range. For bright active regions, unocculted ones lead to shallower, occulted ones to deeper transits. If a star has an activity belt like the Sun, it depends on where a planet transits if the observed absorption is deeper or shallower than assuming a homogeneous disk. For the case of HD 189733b, Llama & Shkolnik (2016) state that other studies found no bumps in lightcurves, i.e. no spot crossings, so the planet is unlikely to transit an active belt (if the star actually has one). Since unocculted regions make a transit shallower, it is possible that the 2010 observations were affected by an increased number of unocculted active regions. However, we remind that the planetary absorption in Ly α can only be studied in the line wings due to geocoronal emission and ISM absorption. The wings of the Ly α line show a much more homogeneous activity pattern than the core, since they are formed at lower temperatures deeper in the chromosphere (Salz et al. 2016a).

For the second effect, Llama & Shkolnik (2016) simulated transits in light curves of the disk-integrated solar Ly α line flux. Although the recovered planetary radii can be up to 50% larger for solar-like variability, they found that the effect is unlikely to be responsible for the strong transit absorptions detected on stars like HD 189733b, even if the solar variability is scaled up in amplitude.

7. Conclusions

We model the Ly α transit absorption of the hot Jupiter HD 189733b using a 1D hydrodynamic code for the upper atmosphere and a 3D MHD code for the planetary-stellar wind interaction and related production of ENAs. We find that the transit absorption observed in 2011 can be reproduced **reasonably well** with typical stellar XUV conditions ($F_{\text{XUV}} \sim 1.8 \times 10^4 \text{ erg cm}^{-2} \text{ s}^{-1}$). The influence of enhanced stellar irradiation during a flare similar to the one observed about 8 h before the transit in 2011 is too small to significantly affect the neutral hydrogen outflow rates. Moreover, we find **with our modeling approach** that the absorption signature is dominated by the atmospheric neutral hydrogen and that the ENAs produced by charge-exchange with the stellar wind **have a negligibly small effect, as they are produced inside the bow shock and have small velocities and high temperatures due to the stellar wind deceleration at the planetary obstacle. Moreover, we find no differences in planetary absorption for all tested stellar wind cases, including the CME event.** This raises the question if the 2010 non-detection was actually “anomalous”, and not the absorption signature detected in 2011, as previously suggested. The variation between the two observations may have been related to significant differences in stellar activity, by magnitude or spectral shape (Guo & Ben-Jaffel 2016), or its variability (Llama & Shkolnik 2016). Observations of this system in Ly α at a further epoch, preferentially with simultaneous X-ray monitoring to constrain the stellar XUV emission, would help to clarify this issue.

Acknowledgements. We thank the referee for valuable comments and suggestions. We thank A. Vidotto for providing the modeled stellar wind parameters.

This work was supported by the Austrian Science Fund (FWF) project P27256-N27 “Characterizing Stellar and Exoplanetary Environments via Modeling of Lyman- α Transit Observations of Hot Jupiters”. The authors further acknowledge the support by the FWF NFN project S11601-N16 “Pathways to Habitability: From Disks to Active Stars, Planets and Life”, and the related FWF NFN subproject S11607-N16 “Particle/Radiative Interactions with Upper Atmospheres of Planetary Bodies Under Extreme Stellar Conditions” (KK, HL, NVE), as well as FWF projects P30949-N36 (PO, ML) and I2939-N27. LF, DK and NVE acknowledge also the Austrian Forschungsförderungsgesellschaft FFG project “TAPAS4CHEOPS” P853993. NVE and VAI acknowledge support by the Russian Science Foundation grant No 18-12-00080.

References

- Adams, F. C. 2011, *ApJ*, 730, 27
 Alvarado-Gómez, J. D., Drake, J. J., Cohen, O., Moschou, S. P., & Garraffo, C. 2018, *ApJ*, 862, 93
 Bakos, G. Á., Pál, A., Latham, D. W., Noyes, R. W., & Stefanik, R. P. 2006, *ApJ*, 641, L57
 Ballester, G. E. & Ben-Jaffel, L. 2015, *ApJ*, 804, 116
 Ballester, G. E., Sing, D. K., & Herbert, F. 2007, *Nature*, 445, 511
 Barnes, J. R., Haswell, C. A., Staab, D., & Anglada-Escudé, G. 2016, *MNRAS*, 462, 1012
 Ben-Jaffel, L. 2007, *ApJ*, 671, L61
 Ben-Jaffel, L. 2008, *ApJ*, 688, 1352
 Ben-Jaffel, L. & Ballester, G. E. 2013, *A&A*, 553, A52
 Ben-Jaffel, L. & Sona Hosseini, S. 2010, *ApJ*, 709, 1284
 Bisikalo, D., Kaygorodov, P., Ionov, D., et al. 2013, *ApJ*, 764, 19
 Bouchy, F., Udry, S., Mayor, M., et al. 2005, *A&A*, 444, L15
 Bourrier, V., Ehrenreich, D., & Lecavelier des Etangs, A. 2015, *A&A*, 582, A65
 Bourrier, V. & Lecavelier des Etangs, A. 2013, *A&A*, 557, A124
 Bourrier, V., Lecavelier des Etangs, A., Dupuy, H., et al. 2013, *A&A*, 551, A63
 Bourrier, V., Lecavelier des Etangs, A., Ehrenreich, D., Tanaka, Y. A., & Vidotto, A. A. 2016, *A&A*, 591, A121
 Cauley, P. W., Redfield, S., & Jensen, A. G. 2017a, *AJ*, 153, 217
 Cauley, P. W., Redfield, S., & Jensen, A. G. 2017b, *AJ*, 153, 185
 Cauley, P. W., Redfield, S., Jensen, A. G., & Barman, T. 2016, *AJ*, 152, 20
 Cauley, P. W., Redfield, S., Jensen, A. G., et al. 2015, *ApJ*, 810, 13
 Chadney, J. M., Galand, M., Unruh, Y. C., Koskinen, T. T., & Sanz-Forcada, J. 2015, *Icarus*, 250, 357
 Chadney, J. M., Koskinen, T. T., Galand, M., Unruh, Y. C., & Sanz-Forcada, J. 2017, *A&A*, 608, A75
 Christie, D., Arras, P., & Li, Z.-Y. 2016, *ApJ*, 820, 3
 Cohen, O., Kashyap, V. L., Drake, J. J., et al. 2011, *ApJ*, 733, 67
 Davis, S. F. 1984, *ICASE Report*, 84-20, 1
 de Kok, R. J., Brogi, M., Snellen, I. A. G., et al. 2013, *A&A*, 554, A82
 Debrecht, A., Carroll-Nellenback, J., Frank, A., et al. 2018, *MNRAS*, 478, 2592
 Drake, J. J., Cohen, O., Yashiro, S., & Gopalswamy, N. 2013, *ApJ*, 764, 170
 Eggleton, P. P. 1983, *ApJ*, 268, 368
 Ehrenreich, D., Bourrier, V., Bonfils, X., et al. 2012, *A&A*, 547, A18
 Ehrenreich, D., Bourrier, V., Wheatley, P. J., et al. 2015, *Nature*, 522, 459
 Ehrenreich, D., Lecavelier Des Etangs, A., Hébrard, G., et al. 2008, *A&A*, 483, 933
 Ekenbäck, A., Holmström, M., Wurz, P., et al. 2010, *ApJ*, 709, 670
 Erkaev, N. V., Kulikov, Y. N., Lammer, H., et al. 2007, *A&A*, 472, 329
 Erkaev, N. V., Lammer, H., Odert, P., et al. 2016, *MNRAS*, 460, 1300
 Erkaev, N. V., Lammer, H., Odert, P., Kulikov, Y. N., & Kislyakova, K. G. 2015, *MNRAS*, 448, 1916
 Erkaev, N. V., Lammer, H., Odert, P., et al. 2013, *Astrobiology*, 13, 1011
 Erkaev, N. V., Odert, P., Lammer, H., et al. 2017, *MNRAS*, 470, 4330
 Fares, R., Donati, J.-F., Moutou, C., et al. 2010, *MNRAS*, 406, 409
 Fossati, L., Haswell, C. A., Froning, C. S., et al. 2010, *ApJ*, 714, L222
 France, K., Froning, C. S., Linsky, J. L., et al. 2013, *ApJ*, 763, 149
 Gaia Collaboration, Brown, A. G. A., Vallenari, A., et al. 2016, *A&A*, 595, A2
 García Muñoz, A. 2007, *Planet. Space Sci.*, 55, 1426
 Glaister, P. 1991a, *Computers Math. Applic.*, 21, 39
 Glaister, P. 1991b, *Computers Math. Applic.*, 22, 45
 Glover, S. C. O. & Jappsen, A.-K. 2007, *ApJ*, 666, 1
 Gray, R. O., Corbally, C. J., Garrison, R. F., McFadden, M. T., & Robinson, P. E. 2003, *AJ*, 126, 2048
 Güdel, M., Audard, M., Kashyap, V. L., Drake, J. J., & Guinan, E. F. 2003, *ApJ*, 582, 423
 Guo, J. H. 2011, *ApJ*, 733, 98
 Guo, J. H. 2013, *ApJ*, 766, 102
 Guo, J. H. & Ben-Jaffel, L. 2016, *ApJ*, 818, 107
 Haswell, C. A., Fossati, L., Ayres, T., et al. 2012, *ApJ*, 760, 79
 Henry, G. W. & Winn, J. N. 2008, *AJ*, 135, 68
 Holmström, M., Ekenbäck, A., Selsis, F., et al. 2008, *Nature*, 451, 970

- Huebner, W. F. & Mukherjee, J. 2015, *Planet. Space Sci.*, 106, 11
- Hünsch, M., Schmitt, J. H. M. M., Sterzik, M. F., & Voges, W. 1999, *A&AS*, 135, 319
- Ionov, D. & Shematovich, V. 2015, *Solar System Research*, 49, 339
- Jensen, A. G., Redfield, S., Endl, M., et al. 2012, *ApJ*, 751, 86
- Käppeli, R. & Mishra, S. 2016, *A&A*, 587, A94
- Khodachenko, M. L., Lammer, H., Lichtenegger, H. I. M., et al. 2007, *Planet. Space Sci.*, 55, 631
- Khodachenko, M. L., Shaikhislamov, I. F., Lammer, H., et al. 2017, *ApJ*, 847, 126
- Khodachenko, M. L., Shaikhislamov, I. F., Lammer, H., & Prokopenko, P. A. 2015, *ApJ*, 813, 50
- Kislyakova, K. G., Holmström, M., Lammer, H., Odert, P., & Khodachenko, M. L. 2014, *Science*, 346, 981
- Kohl, S., Salz, M., Czesla, S., & Schmitt, J. H. M. M. 2018, *A&A*, 619, A96
- Koskinen, T. T., Harris, M. J., Yelle, R. V., & Lavvas, P. 2013, *Icarus*, 226, 1678
- Kulow, J. R., France, K., Linsky, J., & Loyd, R. O. P. 2014, *ApJ*, 786, 132
- Lara, A., Gonzalez-Esparza, J. A., & Gopalswamy, N. 2004, *Geofisica Internacional*, 43, 75
- Lavie, B., Ehrenreich, D., Bourrier, V., et al. 2017, *A&A*, 605, L7
- Lecavelier des Etangs, A., Bourrier, V., Wheatley, P. J., et al. 2012, *A&A*, 543, L4
- Lecavelier des Etangs, A., Ehrenreich, D., Vidal-Madjar, A., et al. 2010, *A&A*, 514, A72
- Leitzinger, M., Odert, P., Greimel, R., et al. 2014, *MNRAS*, 443, 898
- Leitzinger, M., Odert, P., Greimel, R., et al. 2020, *MNRAS*, in press [[arXiv:2002.04430](https://arxiv.org/abs/2002.04430)]
- Lindsay, B. G. & Stebbings, R. F. 2005, *Journal of Geophysical Research (Space Physics)*, 110, A12213
- Linsky, J. L., Fontenla, J., & France, K. 2014, *ApJ*, 780, 61
- Linsky, J. L., Yang, H., France, K., et al. 2010, *ApJ*, 717, 1291
- Llama, J. & Shkolnik, E. L. 2015, *ApJ*, 802, 41
- Llama, J. & Shkolnik, E. L. 2016, *ApJ*, 817, 81
- Llama, J., Vidotto, A. A., Jardine, M., et al. 2013, *MNRAS*, 436, 2179
- MacCormack, R. W. 1969, *AIAA*, Paper 69-354,
- MacCormack, R. W. 1971, in *Lecture Notes in Physics*, Berlin Springer Verlag, Vol. 8, *Numerical Methods in Fluid Dynamics* Numerical Methods in Fluid Dynamics, ed. M. Holt, 151–163
- Marin, F. & Grosso, N. 2017, *ApJ*, 835, 283
- Matsakos, T., Uribe, A., & Königl, A. 2015, *A&A*, 578, A6
- Menager, H., Barthélemy, M., Koskinen, T., et al. 2013, *Icarus*, 226, 1709
- Murray-Clay, R. A., Chiang, E. I., & Murray, N. 2009, *ApJ*, 693, 23
- Odert, P., Leitzinger, M., Guenther, E. W., & Heinzel, P. 2019, *MNRAS*, submitted
- Odert, P., Leitzinger, M., Hansmeier, A., & Lammer, H. 2017, *MNRAS*, 472, 876
- Owen, J. E. & Adams, F. C. 2014, *MNRAS*, 444, 3761
- Patsourakos, S. & Georgoulis, M. K. 2016, *A&A*, 595, A121
- Peebles, P. J. E. 1993, *Principles of Physical Cosmology* (Princeton University Press)
- Penz, T., Erkaev, N. V., Kulikov, Y. N., et al. 2008, *Planet. Space Sci.*, 56, 1260
- Petit, P., Louge, T., Théado, S., et al. 2014, *PASP*, 126, 469
- Pillitteri, I., Günther, H. M., Wolk, S. J., Kashyap, V. L., & Cohen, O. 2011, *ApJ*, 741, L18
- Pillitteri, I., Maggio, A., Micela, G., et al. 2015, *ApJ*, 805, 52
- Pillitteri, I., Wolk, S. J., Cohen, O., et al. 2010, *ApJ*, 722, 1216
- Pillitteri, I., Wolk, S. J., Lopez-Santiago, J., et al. 2014, *ApJ*, 785, 145
- Poppenhaeger, K., Schmitt, J. H. M. M., & Wolk, S. J. 2013, *ApJ*, 773, 62
- Poppenhaeger, K. & Wolk, S. J. 2014, *A&A*, 565, L1
- Route, M. 2019, *ApJ*, 872, 79
- Salz, M., Czesla, S., Schneider, P. C., & Schmitt, J. H. M. M. 2016a, *A&A*, 586, A75
- Salz, M., Schneider, P. C., Czesla, S., & Schmitt, J. H. M. M. 2016b, *A&A*, 585, L2
- Sanz-Forcada, J., García-Álvarez, D., Velasco, A., et al. 2010, in *IAU Symposium*, Vol. 264, *IAU Symposium*, ed. J.-P. R. A. G. Kosovichev, A. H. Andrei, 478–483
- Sanz-Forcada, J., Micela, G., Ribas, I., et al. 2011, *A&A*, 532, A6
- Schwartz, J. C., Kashner, Z., Jovmir, D., & Cowan, N. B. 2017, *ApJ*, 850, 154
- Schwenn, R., Raymond, J. C., Alexander, D., et al. 2006, *Space Sci. Rev.*, 123, 127
- Sekiya, M., Nakazawa, K., & Hayashi, C. 1980, *Prog. Theor. Phys.*, 64, 1968
- Semelin, B., Combes, F., & Baek, S. 2007, *A&A*, 474, 365
- Shaikhislamov, I. F., Khodachenko, M. L., Lammer, H., et al. 2016, *ApJ*, 832, 173
- Shaikhislamov, I. F., Khodachenko, M. L., Sasunov, Y. L., et al. 2014, *ApJ*, 795, 132
- Shematovich, V. I., Ionov, D. E., & Lammer, H. 2014, *A&A*, 571, A94
- Stassun, K. G., Collins, K. A., & Gaudi, B. S. 2017, *AJ*, 153, 136
- Stone, J. M. & Proga, D. 2009, *ApJ*, 694, 205
- Tian, F., Toon, O. B., Pavlov, A. A., & De Sterck, H. 2005, *ApJ*, 621, 1049
- Tilley, M. A., Harnett, E. M., & Winglee, R. M. 2016, *ApJ*, 827, 77
- Trammell, G. B., Arras, P., & Li, Z.-Y. 2011, *ApJ*, 728, 152
- Trammell, G. B., Li, Z.-Y., & Arras, P. 2014, *ApJ*, 788, 161
- Tremblin, P. & Chiang, E. 2013, *MNRAS*, 428, 2565
- Verner, D. A., Ferland, G. J., Korista, K. T., & Yakovlev, D. G. 1996, *ApJ*, 465, 487
- Vidal-Madjar, A., Désert, J., Lecavelier des Etangs, A., et al. 2004, *ApJ*, 604, L69
- Vidal-Madjar, A., Huitson, C. M., Bourrier, V., et al. 2013, *A&A*, 560, A54
- Vidal-Madjar, A., Lecavelier des Etangs, A., Désert, J., et al. 2008, *ApJ*, 676, L57
- Vidal-Madjar, A., Lecavelier des Etangs, A., Désert, J.-M., et al. 2003, *Nature*, 422, 143
- Waite, J. H., Cravens, T. E., Kozyra, J., et al. 1983, *J. Geophys. Res.*, 88, 6143
- Wood, B. E. 2004, *Living Rev. Sol. Phys.*, 1, 2
- Yashiro, S. & Gopalswamy, N. 2009, in *IAU Symposium*, Vol. 257, *Universal Heliophysical Processes*, ed. N. Gopalswamy & D. F. Webb, 233–243
- Yashiro, S., Gopalswamy, N., Michalek, G., et al. 2004, *J. Geophys. Res.*, 109, A07105
- Yelle, R. V. 2004, *Icarus*, 170, 167

Appendix A: MacCormack TVD scheme

The hydrodynamic model, as described in Erkaev et al. (2016), solves the set of 1D hydrodynamic equations using the MacCormack scheme (MacCormack 1969) which is second order accurate in space and time. This scheme is well-suited for supersonic outflows, but may experience instabilities and oscillations if the outflows are largely subsonic, as in the case of the high-gravity planet HD 189733b. Several studies developed corrections to the original MacCormack scheme to give it Total Variation Diminishing (TVD) properties (e.g. Davis 1984). This suppresses spurious numerical oscillations, which may occur at steep gradients and destabilize the code. Specifically, we adopt the method of Glaister (1991b) designed for non-uniform grids (Glaister 1991a).

The system of hydrodynamic equations (Eqs. 1-3) is first normalized as described in (Erkaev et al. 2016) and then written in vector form

$$\frac{\partial U}{\partial t} + \frac{\partial F}{\partial r} = S, \quad (\text{A.1})$$

where U is the vector of the variables, F the fluxes and S the source terms. Here,

$$U = \begin{pmatrix} \rho r^2 \\ \rho u r^2 \\ E_{\text{th}} r^2 \end{pmatrix}, F = \begin{pmatrix} \rho u r^2 \\ (\rho u^2 + p) r^2 \\ E_{\text{th}} u r^2 \end{pmatrix}, S = \begin{pmatrix} 0 \\ g \rho r^2 + 2 p r \\ Q_{\text{net}} r^2 - p \frac{\partial u r^2}{\partial r} \end{pmatrix}. \quad (\text{A.2})$$

The MacCormack method consists of a predictor step

$$U_i^{n+1/2} = U_i - \Delta t \frac{F_{i+1}^n - F_i^n}{r_{i+1} - r_i} + \Delta t S_i^n \quad (\text{A.3})$$

and a corrector step

$$U_i^{n+1} = \frac{1}{2} (U_i^n + U_i^{n+1/2}) - \frac{\Delta t}{2} \frac{F_i^{n+1/2} - F_{i-1}^{n+1/2}}{r_i - r_{i-1}} + \frac{\Delta t}{2} S_i^{n+1/2}, \quad (\text{A.4})$$

where the indices i and n refer to spatial and temporal steps, respectively. The superscript $n+1/2$ refers to quantities evaluated after the predictor step. The time step is updated according to the Courant-Friedrichs-Lewy condition $\Delta t = C_{\text{CFL}} \Delta x_{\text{min}} / (|u| + c)_{\text{max}}$, where Δx_{min} is the smallest grid size, c is the adiabatic sound speed, $(|u| + c)_{\text{max}}$ is the maximum wave speed on the grid, and $C_{\text{CFL}} \leq 1$ is the Courant-Friedrichs-Lewy number, which we take to be 0.8.

Here we newly implement the improved scheme of MacCormack (1971) for solving the momentum equation. This is related to the destabilizing effect of cases where the velocities $u_i < 0$ and $u_{i+1} > 0$. Since the momentum flux ρu^2 loses the information on the sign of u , MacCormack (1971) suggested is such cases to replace the momentum flux differences $(\rho u^2)_{i+1} - (\rho u^2)_i$ with $[(\rho u)_{i+1} - (\rho u)_i](u_{i+1} + u_i)/2$ in Eq. A.3, and with correspondingly adjusted indices in Eq. A.4. This preserves the sign of the flux and removes instabilities.

The TVD corrections from Glaister (1991b) are implemented as follows. After every corrector step, TVD correction terms are added to the solution,

$$U_{i,\text{TVD}}^{n+1} = U_i^{n+1} + \left[\hat{K}_{i+1/2}^+ + \hat{K}_{i+1/2}^- \right] \frac{\Delta U_{i+1/2}^n}{\Delta r_i} - \left[\hat{K}_{i-1/2}^+ + \hat{K}_{i-1/2}^- \right] \frac{\Delta U_{i-1/2}^n}{\Delta r_i}, \quad (\text{A.5})$$

where $\Delta U_{i+1/2}^n = U_{i+1}^n - U_i^n$, $\Delta U_{i-1/2}^n = U_i^n - U_{i-1}^n$, and $\Delta r_i = (r_{i+1} - r_{i-1})/2$. The coefficients \hat{K} are determined with

$$\hat{K}_{i\pm 1/2}^\pm = \frac{1}{2} |\lambda_{i\pm 1/2}|_{\text{max}} \Delta t \left(1 - |\lambda_{i\pm 1/2}|_{\text{max}} \frac{\Delta t}{\Delta r_{i\pm 1/2}} \right) (1 - \psi(M_{i\pm 1/2}^\pm)), \quad (\text{A.6})$$

where $|\lambda_{i\pm 1/2}|_{\text{max}} = |u_{i\pm 1/2}| + c_{i\pm 1/2}$ is the maximum local wave speed and $\psi(M) = \max(0, \min(1, M))$ is the minmod limiter. The coefficients M^\pm are calculated via

$$M_{i\pm 1/2}^\pm = \frac{\left(\frac{y_{i\pm 1/2}^\pm}{\Delta r_{i\pm 1/2}} - |\lambda_{i\pm 1/2}^\pm|_{\text{max}} \frac{\Delta t}{\Delta r_{i\pm 1/2}} \right) (\Delta U_{i\pm 1/2}^n \cdot \Delta U_{i\pm 1/2}^n)}{\left(1 - |\lambda_{i\pm 1/2}^\pm|_{\text{max}} \frac{\Delta t}{\Delta r_{i\pm 1/2}} \right) (\Delta U_{i\pm 1/2}^n \cdot \Delta U_{i\pm 1/2}^n)}, \quad (\text{A.7})$$

where s denotes the sign function of the superscript⁵ and the expression $(* \cdot *)$ refers to the inner product of the difference vectors ΔU . The parameter

$$y_{i\pm 1/2}^\pm = \frac{\Delta r_{i\pm 1/2+s}}{\Delta r_{i\pm 1/2}} \quad (\text{A.8})$$

is the ratio of successive grid spacings.

Appendix A.1: Other modifications

Due to the highly subsonic nature of the outflow for planets with high gravity, the solution of the velocity profile is affected by unphysical behavior (negative values, increasing u towards the planet) close to the lower boundary of the computational domain. The situation improves when the code is run for very long times (because of the small timesteps), which is inconvenient. The problem is (partly) due to the solution method. We then tried to solve the momentum equation in non-conservative form treating both the pressure and gravity terms as source terms, i.e. the vector components (Eq. A.2) are modified to $F_2 = \rho u^2 r^2$ and $S_2 = -\rho r^2 \partial \Phi / \partial r - r^2 \partial p / \partial r$. In the limit of $u \rightarrow 0$, hydrostatic equilibrium should be reached and the two terms in S_2 should cancel. Schemes which maintain hydrostatic equilibrium in this limit are called well-balanced schemes. We modify the discretization of the source terms according to the suggestions of Käppeli & Mishra (2016). First, the derivatives of Φ and p in S_2 are discretized the same way as the respective advection terms in Eqs. A.3 and A.4; second, the prefactors of these derivatives (ρr^2 , r^2) are calculated as averages of their values at the grid points involved in the derivatives. For Eq. A.3, this yields

$$-\frac{(\rho r^2)_{i+1} + (\rho r^2)_i}{2} \frac{\Phi_{i+1} - \Phi_i}{r_{i+1} - r_i} - \frac{(r^2)_{i+1} + (r^2)_i}{2} \frac{p_{i+1} - p_i}{r_{i+1} - r_i}, \quad (\text{A.9})$$

and similar for Eq. A.4 with correspondingly adjusted indices. This procedure improved the resulting velocity profiles. We checked that this implementation does not affect the results by comparing runs for a lower gravity planet (where this modification is not necessary) using both the conservative and the modified formulation of the momentum equation.

Appendix A.2: Mass and energy conservation

Figure A.1 shows the mass flux $\rho u r^2$ normalized to its value at the upper boundary as a function of r , as well as the total heating and cooling rates for the SF11 run. One can see that both

⁵ Meaning $s = 1$ for superscript “+” and $s = -1$ for superscript “-”.

mass and energy are well conserved in our model. We adopt the convergence criterion that the momentum flux should be conserved to 1% throughout the domain. This is only violated close to the planetary surface where the very subsonic velocities introduce numerical difficulties for this planet. Also the total heating and cooling rates agree well, indicating good energy conservation properties of the code, except close to the planet where the numerical errors lead to slightly lower adiabatic cooling than expected.

Appendix B: Comparison of 1D and 2D heating

Figure B.1 shows a comparison between Eq. 13 and the 2D heating function (e.g. Erkaev et al. 2016). For the latter it is assumed that the density profile along the star-planet line is valid for all other directions. This is approximately valid if the Roche lobe is far from the planet and the planet is not tidally locked so that the stellar XUV flux is distributed efficiently over the whole atmosphere. However, for a hot Jupiter, these assumptions are likely not valid and a fully 3D model would be needed. Moreover, since we introduced a wavelength dependent heating function here which raises the computational demand, we use a 1D heating function. Adopting the neutral hydrogen density profile from the SF11 run, we a posteriori calculate the 2D volume heating rate and compare it with Eq. 13. One can see that for the adopted planetary and stellar parameters, $\alpha = 4$ represents the best match and was consequently used in all runs.

Appendix C: Molecular hydrogen

Here we test if neglecting molecular hydrogen could have an impact on the results. We calculate the equilibrium abundance of H_2 , which can be justified considering that it will only be abundant close to R_p where velocities are very small, after

$$n_{\text{H}_2} = \frac{\gamma_{\text{H}} n_{\text{H}}^2}{\nu_{\text{H}_2} + \nu_{\text{diss}} n}, \quad (\text{C.1})$$

where $\gamma_{\text{H}} = 8 \times 10^{-33} (300/T)^{0.6}$ is the rate of the reaction producing H_2 ($\text{H}+\text{H}\rightarrow\text{H}_2$) and $\nu_{\text{diss}} = 1.5 \times 10^{-9} \exp(-49000/T)$ the thermal dissociation rate (Yelle 2004; Erkaev et al. 2016). The photoionization rate ν_{H_2} is calculated after Eq. 6, but replacing σ_{ion} with that for H_2 (Huebner & Mukherjee 2015). The resulting number density profile of H_2 , along with the densities of H atoms and protons for the SF11 run are shown in Fig. C.1. One can see that H_2 would only be the dominating species at distances $\lesssim 1.04R_p$, very close to the optical radius. The main part of the upper atmosphere is composed of H and H^+ . This is consistent with Guo & Ben-Jaffel (2016) who found the same H_2/H transition radius with their hydrodynamic model (which does include H-chemistry) and that the planetary wind is dominated by H and H^+ . Therefore, we do not expect that inclusion of H_2 would noticeably change our results.

Appendix D: Stellar wind parameters

In Fig. D.1 we show the stellar wind parameters along the orbit based on the magnetic field map (Fares et al. 2010) and a 3D wind model (Llama et al. 2013).

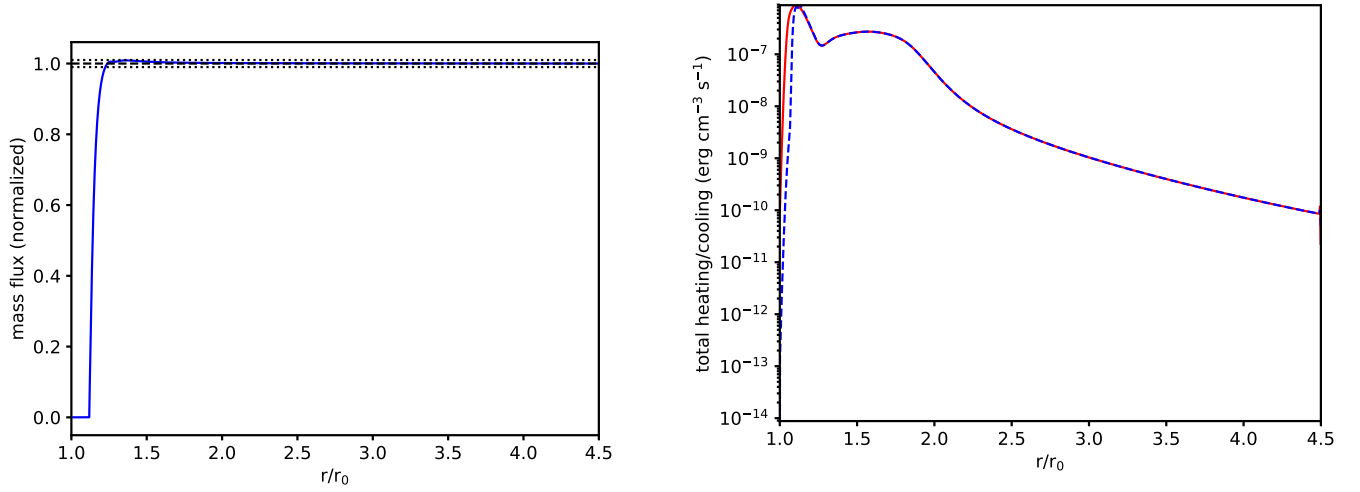


Fig. A.1. Demonstration of the conservation properties our code in a converged solution (SF11 run). Left: normalized mass flux (blue), the dashed and dotted black lines indicate unity and $\pm 1\%$, respectively. Right: total heating (red) and cooling rates (dashed blue).

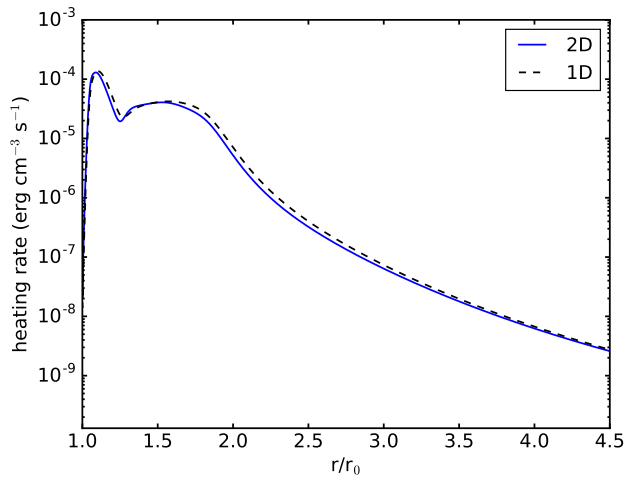


Fig. B.1. Comparison of 2D and 1D XUV volume heating rates.

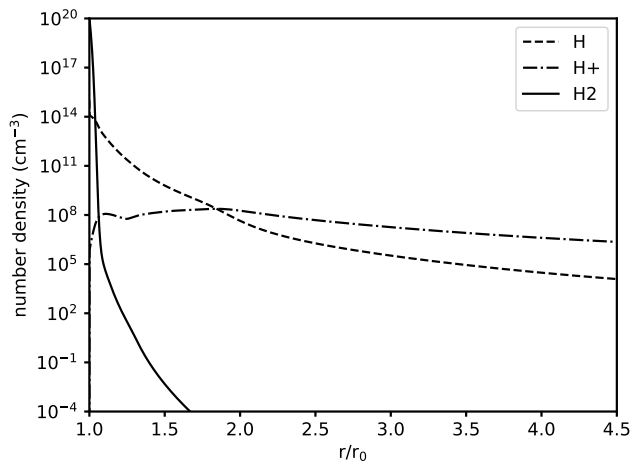


Fig. C.1. Number densities of H₂, H and H⁺, where the latter two are taken from the SF11 run and the H₂ density is calculated from Eq. C.1.

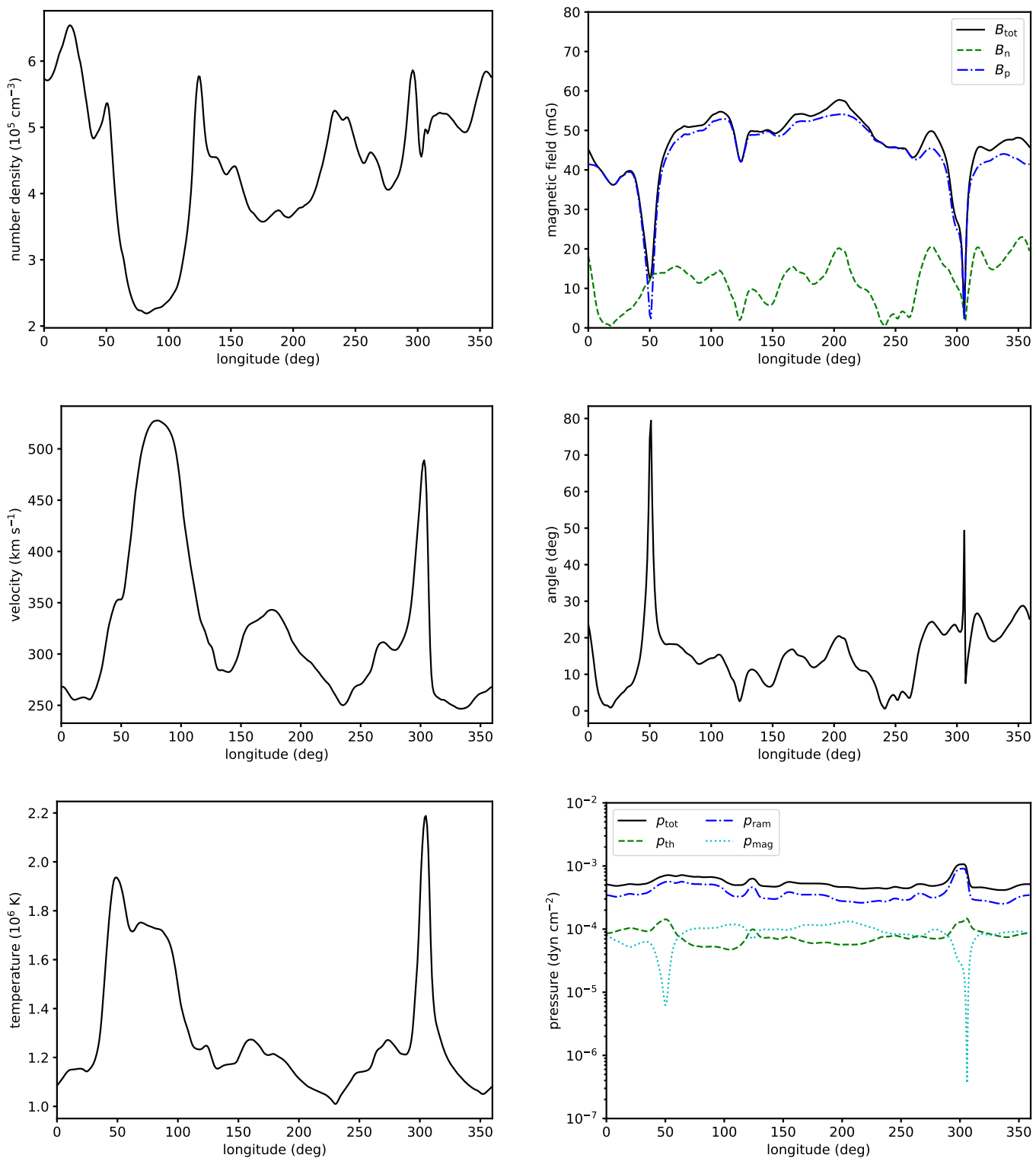


Fig. D.1. Variation of the stellar wind parameters along the orbit of HD 189733b. Shown are the number density, velocity, temperature, strength of the total magnetic field and its components (parallel and normal to V_{sw}), the angle between the magnetic field and the star–planet line, and the total pressure with its components (thermal, magnetic, and ram pressures).